

A graphical multi-fidelity Gaussian process model, with application to emulation of expensive computer simulations

Yi Ji¹, Simon Mak¹, Derek Soeder², J-F Paquet², and Steffen A. Bass²

¹Department of Statistical Science, Duke University, Durham, North Carolina

²Department of Physics, Duke University, Durham, North Carolina

June 4, 2025

Abstract

With advances in scientific computing and mathematical modeling, complex phenomena can now be reliably simulated. Such simulations can however be very time-intensive, requiring millions of CPU hours to perform. One solution is multi-fidelity emulation, which uses data of varying accuracies (or fidelities) to train an efficient predictive model (or emulator) for the expensive simulator. In complex problems, simulation data with different fidelities are often connected scientifically via a directed acyclic graph (DAG), which cannot be integrated within existing multi-fidelity emulator models. We thus propose a new Graphical Multi-fidelity Gaussian process (GMGP) model, which embeds this scientific DAG information within a Gaussian process framework. We show that the GMGP has desirable modeling traits via two Markov properties, and admits a scalable formulation for recursively computing the posterior predictive distribution along sub-graphs. We also present an experimental design framework over the DAG given a computational budget, and propose a nonlinear extension of the GMGP model via deep Gaussian processes. The advantages of the GMGP model over existing methods are then demonstrated via a suite of numerical experiments and an application to emulation of heavy-ion collisions, which can be used to study the conditions of matter in the Universe shortly after the Big Bang.

Keywords: Computer experiments, graphical models, heavy-ion physics, Gaussian processes, multi-fidelity modeling.

1 Introduction

With recent breakthroughs in scientific computing, computer simulations are quickly replacing physical experiments in modern scientific and engineering problems. These simulations allow scientists to better understand complex scientific problems which may be prohibitively expensive or infeasible for direct experimentation. This shift to *computer* experimentation has found success in many exciting applications, including rocket design (Mak et al., 2018), cosmological expansion (Kaufman et al., 2011) and machining of metals (Hung et al., 2015). These computer experiments, however, can demand a hefty price in computational resources, requiring millions of CPU hours per run. One solution is *emulation* (Santner et al., 2003): a handful of simulations are first run at carefully chosen design points, then an *emulator* model is fit to efficiently predict the expensive computer simulator. A popular emulator model is the Gaussian process (GP) model (Santner et al., 2003), which allows for closed-form expressions for prediction and uncertainty quantification.

As systems become more realistic and complex, however, computer experiments also become increasingly more expensive, and thus the simulation data needed to train an accurate emulator can be difficult to generate. One way to address this is *multi-fidelity emulation*. The idea is to collect data from the “high-fidelity” simulator, which is computationally *expensive* but provides a detailed representation of the modeled science, as well as data from “lower-fidelity” simulators, which make simplifying assumptions on the modeled science but can be performed *quickly*. One then fits a *multi-fidelity* emulator using all training data to predict the output from the high-fidelity simulator. The key advantage of multi-fidelity emulation is that, by leveraging information from cheaper lower-fidelity simulations to enhance predictions for the high-fidelity model, one can train a predictive model with much fewer high-fidelity simulations and thereby lower computational costs.

The development of multi-fidelity emulators is an active research area. A popular

framework is the Kennedy-O’Hagan (KO) model (Kennedy and O’Hagan, 2000), which models a sequence of computer simulations from lowest to highest fidelity using a sequence of GP models linked by a linear autoregressive framework. The KO multi-fidelity model has been applied in a wide range of scientific problems, such as materials science (Pilania et al., 2017) and aerodynamics (López-Lopera et al., 2021). For efficient prediction, Le Gratiet and Garnier (2014) proposed a reformulation of the KO model which allows for a recursive computation of the predictive distribution. Perdikaris et al. (2017) presented a more flexible, nonlinear formulation of the KO model using deep GPs (Damianou and Lawrence, 2013). Inference on model parameters has also been considered in different ways. Qian and Wu (2008) and Le Gratiet (2013) proposed Bayesian formulations of the KO model to account for parameter uncertainties. Ma (2020) presented an objective Bayesian formulation of this model and derived closed-form posterior predictive equations that depend only on correlation parameters. A comprehensive review of multi-fidelity emulator models can be found in Fernández-Godino et al. (2016) and Peherstorfer et al. (2018).

However, there is a key limitation of the above methods: they presume the multi-fidelity nature of simulations forms a sequence from lowest to highest fidelity. This may not be the case for complex scientific problems. Take, e.g., the heavy-ion collision framework in Everett et al. (2021b) for simulating the quark-gluon plasma, the state of nuclear matter that once filled the Universe shortly after the Big Bang, and that can now be produced and explored in collisions of heavy nuclei. This simulation consists of three stages, as shown in Figure 1. For each stage, the physicists choose one of several potential models (some more accurate but time-consuming, others less accurate but quick), resulting in many ways to perform the full plasma simulation. Here, it may be difficult to rank different simulation strategies in a sequence from lowest to highest fidelity, since some may be more accurate for one stage but less accurate for another. For example, a physicist may choose the combination $A_1 + B_3 + C_2$ as the high-fidelity simulator H for a study, and use $A_1 + B_1 + C_2$ and $A_1 + B_2 + C_1$ as two

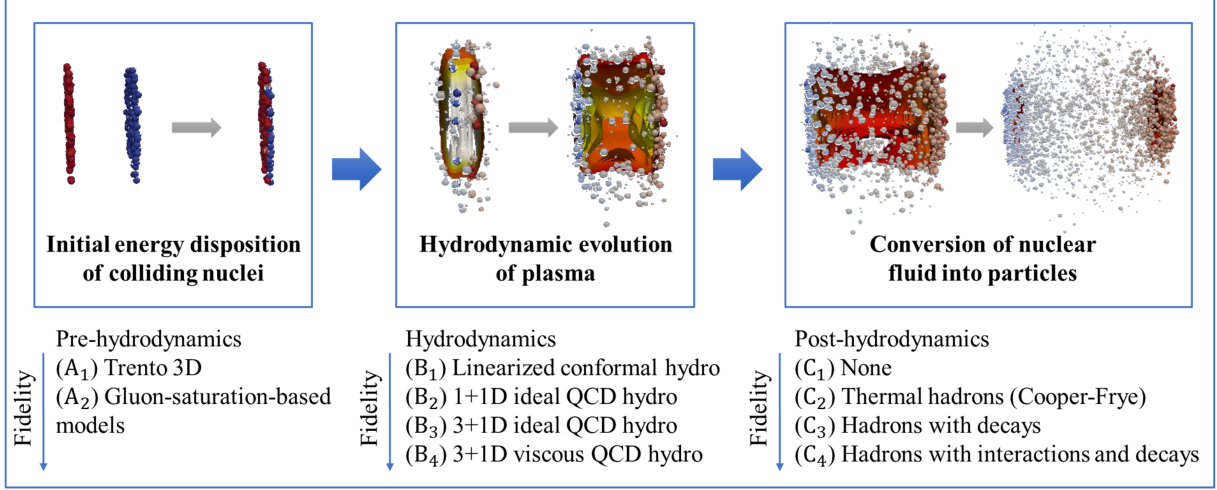


Figure 1: Visualizing the multi-stage multi-fidelity framework for simulating the quark-gluon plasma.

lower-fidelity approximations L_1 and L_2 . To apply existing models, one may have to either (i) *ignore* data from certain simulators to achieve an ordering from lowest to highest fidelity, or (ii) *impose* an artificial ordering which is not justified by the science. As we shall see later, both approaches do not make full use of the underlying multi-fidelity structure, and thus may not achieve good predictive performance given a computational budget.

To address this, we present a new Graphical Multi-fidelity Gaussian process (GMGP) model, which utilizes a directed acyclic graph (DAG) to model inter-dependencies between simulation models of different fidelities. This DAG structure is elicited via a careful inspection of the scientific models, which we discuss later. The GMGP model embeds this DAG within a Gaussian process framework, thus allowing for a more *structured* and *science-driven* approach for pooling information from lower-fidelity simulations to predict a high-fidelity simulator. We show that the GMGP has desirable modeling traits via two Markov properties, and admits an elegant recursive formulation that allows efficient computation of the posterior distribution on sub-graphs. To maximize predictive power, we also present a design framework for allocating experimental runs over the DAG given

a computational budget. Finally, we propose an extension of the GMGP, which models nonlinear dependencies via the embedding of deep Gaussian processes (Damianou and Lawrence, 2013) over the DAG. Simulations and an application to heavy-ion collisions demonstrate the improved performance of the GMGP over existing multi-fidelity models.

The proposed model can be viewed through the broader lens of *science-driven predictive modeling*, which aims to embed known scientific principles as *prior* knowledge for predictive modeling. In recent years, there has been much development on such predictive models for scientific computing, including the integration of scientific information in the form of shape constraints (Golchi et al., 2015; Wang and Berger, 2016), boundary constraints (Ding et al., 2019), spectral information (Chen et al., 2021), and manifold embeddings (Zhang et al., 2021). Here, the GMGP integrates the underlying DAG structure of the multi-fidelity simulators (i.e., the “science”) as prior knowledge within the GP model. As we show later, this integration of scientific knowledge is key for improving predictive accuracy.

We note that, for non-GP-based models, there has been some very recent work (Gorodetsky et al., 2020a,b) which integrates DAG structure for emulation. In particular, these papers focus on linear subspace (e.g., polynomial-based) models, which are popular surrogate models in the applied mathematics literature. Our model has three notable distinctions. First, the GMGP makes use of GPs rather than linear subspace models, which allow for greater *flexibility* and *robustness* in model specification. Second, by leveraging error bounds for GP interpolation, we introduce a novel *design* framework for multi-fidelity experiments which maximizes predictive power given a computational budget. Finally, we provide a *scalable* and *probabilistic* framework for modeling nonlinear linkages using deep GPs, via recursive computation of the posterior predictive distribution on sub-graphs. We demonstrate these three advantages in a suite of numerical experiments and an application.

The paper is organized as follows. Section 2 provides background and motivation. Section 3 presents the GMGP model and its recursive formulation. Section 4 investigates

experimental design approaches. Section 5 introduces a nonlinear extension of the GMGP. Sections 6 and 7 show the effectiveness of the proposed models in a suite of numerical experiments and an application in heavy-ion collisions. Section 8 concludes the paper.

2 Background & Motivation

2.1 Gaussian process modeling

We first provide a brief overview of Gaussian processes (GPs). Let $\mathbf{x} \in \Omega \subseteq \mathbb{R}^d$ be the input parameters for the computer simulator, and $Z(\mathbf{x})$ be its corresponding output. A GP surrogate model places the following prior on the simulation response surface Z :

$$Z(\cdot) \sim \mathcal{GP}(\mu(\cdot), k(\cdot, \cdot)).$$

Here, $\mu(\mathbf{x}) = \mathbb{E}[Z(\mathbf{x})]$ is the mean function of the GP, and $k(\mathbf{x}, \mathbf{x}') = \text{Cov}[Z(\mathbf{x}), Z(\mathbf{x}')] is its covariance function. Without prior knowledge, $\mu(\cdot)$ is typically set as a constant mean μ , and $k(\cdot, \cdot)$ is typically chosen as the squared-exponential or Matérn kernel (see Santner et al., 2003). In what follows, we assume the simulators return *deterministic* outputs (the standard setting for computer experiments), but the proposed models extend analogously to the setting with noisy outputs.$

Suppose that the computer simulator is run at inputs $\mathcal{D} = \{\mathbf{x}_1, \dots, \mathbf{x}_n\}$, yielding simulation outputs $\mathbf{z} = \{Z(\mathbf{x}_1), \dots, Z(\mathbf{x}_n)\}$. Conditioning on this data, the predictive distribution of Z at a new input point \mathbf{x} can be shown to be $[Z(\mathbf{x})|\mathbf{z}, \mathcal{D}] \sim \mathcal{N}(\mu_n(\mathbf{x}), \sigma_n^2(\mathbf{x}))$, with posterior mean and variance:

$$\begin{aligned} \mu_n(\mathbf{x}) &= \mu(\mathbf{x}) + \mathbf{k}(\mathbf{x}, \mathcal{D})^T \mathbf{K}(\mathcal{D})^{-1}(\mathbf{z} - \boldsymbol{\mu}(\mathcal{D})), \\ \sigma_n^2(\mathbf{x}) &= k(\mathbf{x}, \mathbf{x}) - \mathbf{k}(\mathbf{x}, \mathcal{D})^T \mathbf{K}(\mathcal{D})^{-1} \mathbf{k}(\mathbf{x}, \mathcal{D}). \end{aligned} \tag{1}$$

Here, $\mathbf{k}(\mathbf{x}, \mathcal{D}) = [k(\mathbf{x}, \mathbf{x}_1), \dots, k(\mathbf{x}, \mathbf{x}_n)]$ is the vector of covariances, $\boldsymbol{\mu}(\mathcal{D}) = [\mu(\mathbf{x}_1), \dots, \mu(\mathbf{x}_n)]$ is the vector of means, and $\mathbf{K}(\mathcal{D})$ is the covariance matrix for the training data. Equation (1) captures the key advantages of GP-based emulators: the closed-form posterior mean $\mu_n(\mathbf{x})$ provides an efficient *emulator* of the expensive computer simulator, and the closed-form posterior variance $\sigma_n^2(\mathbf{x})$ provides an efficient quantification of its uncertainty.

2.2 The Kennedy-O’Hagan model

A popular model for multi-fidelity emulation is the Kennedy-O’Hagan model (Kennedy and O’Hagan, 2000), which models a sequence of computer codes with increasing fidelity via a sequence of linear autoregressive GP models. Let $\{\mathbf{z}_1, \mathbf{z}_2, \dots, \mathbf{z}_T\}$ denote the training data generated by T levels of code sorted in increasing accuracy, where $\mathbf{z}_t = \{Z_t(\mathbf{x}_i^t)\}_{i=1}^{n_t}$ is the data from the t -th code Z_t . The KO model assumes the multi-fidelity framework:

$$Z_t(\mathbf{x}) = \rho_{t-1} \cdot Z_{t-1}(\mathbf{x}) + \delta_t(\mathbf{x}), \quad Z_{t-1}(\mathbf{x}) \perp \delta_t(\mathbf{x}), \quad t = 2, \dots, T. \quad (2)$$

In words, Equation (2) presumes that, prior to data, the response surface $Z_t(\mathbf{x})$ can be decomposed as the lower-fidelity surface $Z_{t-1}(\mathbf{x})$ times a correlation parameter ρ_{t-1} , plus some discrepancy function $\delta_t(\mathbf{x})$ which models the systematic bias between the two computer simulations. For priors, the first (i.e., lowest-fidelity) surface is assigned a GP prior $Z_1(\mathbf{x}) \sim \mathcal{GP}(\mathbf{h}_1(\mathbf{x})^T \boldsymbol{\beta}_1, \sigma_1^2 r_1(\mathbf{x}, \mathbf{x}'))$, and subsequent discrepancy terms are then assigned independent GP priors $\delta_t(\mathbf{x}) \sim \mathcal{GP}(\mathbf{h}_t(\mathbf{x})^T \boldsymbol{\beta}_t, \sigma_t^2 r_t(\mathbf{x}, \mathbf{x}'))$. Here, the vectors $\mathbf{h}_1(\mathbf{x}), \dots, \mathbf{h}_T(\mathbf{x})$ denote pre-defined basis functions which are used for modeling the prior mean of the GPs, and $\boldsymbol{\beta}_t$ are their associated coefficients.

An important development in the KO model is the recursive formulation proposed by Le Gratiet and Garnier (2014), which reduces computational complexity of the KO model. The key idea is to substitute the GP prior $Z_{t-1}(\mathbf{x})$ in Equation (2) by the *posterior*

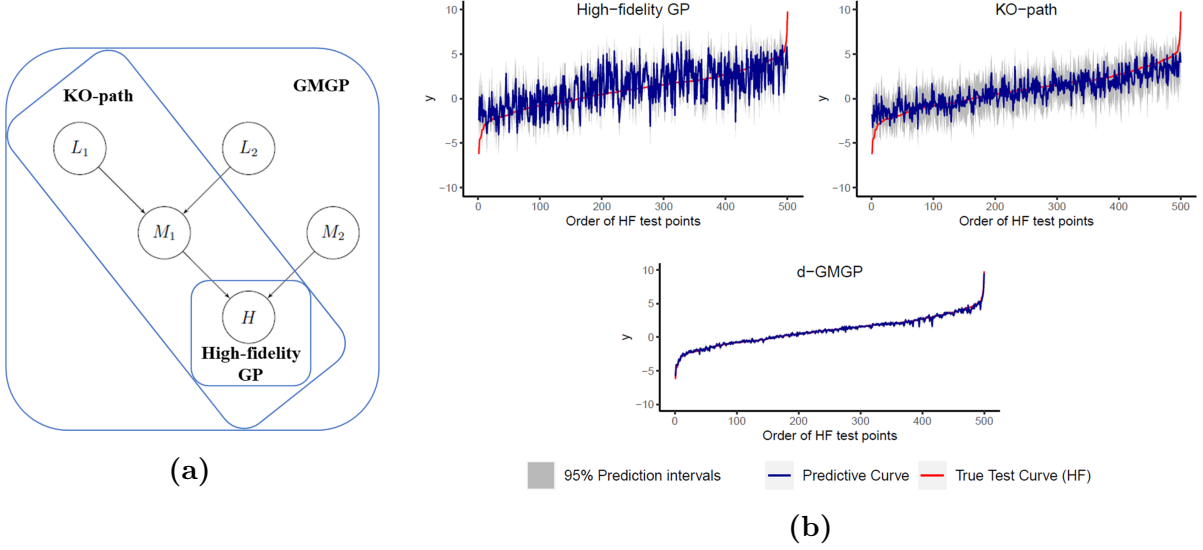


Figure 2: (a) The five-node DAG used in the 20-dimensional test example. (b) Predictive performance of the standard high-fidelity GP model (top left), the KO-path model (top right) and the proposed GMGP model (bottom). Red lines mark the high-fidelity (HF) outputs at test inputs, dark blue lines mark the predicted outputs, and gray bands visualize the 95% predictive intervals.

distribution $Z_{t-1}^*(\mathbf{x}) = [Z_{t-1}(\mathbf{x}) | \mathbf{z}_1, \dots, \mathbf{z}_{t-1}]$, which can be shown to follow a GP. This recursive formulation expresses the predictive mean and variance at level t as functions of the mean and variance at level $t - 1$, which allows for reduced computational cost by avoiding the inversion of large ill-conditioned covariance matrices. With a nested structure for design points, Le Gratiet and Garnier (2014) showed that this recursive formulation yields the same posterior predictive mean and variance as the original KO model, thus justifying the recursive reformulation. Further discussion will be provided later in Section 3.

One limitation of the KO model (and its extensions) is that it presumes the simulations form a *sequence* from lowest to highest fidelity. Consider an example where this may not be the case. We take the $d = 20$ -d test function from Welch et al. (1992) as the high-fidelity simulation response surface, and generate four lower-fidelity representations (details in Section 6). The dependence between these simulators is visualized by the “multi-fidelity DAG” in Figure 2a. The two medium-fidelity codes (M_1 and M_2) are obtained via different

simplifications on the high-fidelity code (H), and the two low-fidelity codes (L_1 and L_2) are obtained by different averaging operations on M_1 . Here, the KO model is unable to capture this underlying multi-fidelity structure, since the five simulators cannot be ranked in a sequence. One way to apply the KO model, which we call the “KO-path model”, is to train it on data along the longest path L_1, M_1, H (see Figure 2a); we will explore alternative ways in Section 6.

Figure 2b shows the predictive performance of the standard GP model trained on 25 design points on H , the KO-path model trained on 25 points on H , 50 points on M_1 and 75 points on L_1 , and the proposed GMGP model trained on the same data with 50 and 75 additional points on M_2 and L_2 . Compared to a standard GP model, the KO-path model appears to provide slightly improved predictive performance. However, the fitted KO model still exhibits poor predictions and high uncertainties over the input space. A natural question is whether we can improve predictive accuracy by integrating the underlying multi-fidelity DAG used for data generation (see Figure 2a). Figure 2b answers this in the affirmative: by integrating the multi-fidelity DAG within an appropriate GP model, the proposed GMGP model yields much better predictive performance over existing methods.

3 The Graphical Multi-fidelity Gaussian Process model

3.1 Model specification

We now present the proposed GMGP model, which generalizes the KO model by embedding the underlying multi-fidelity DAG (capturing scientific dependencies between simulators) as prior information within a GP framework. Let V be the set of nodes representing different simulation codes, and suppose there is a *root* node $T = |V| \in V$ representing the highest-fidelity simulator. Let E be the set of directed edges connecting different simulation codes, where an edge (t', t) is drawn *only* if node t is a *one-step refinement*

of node t' , i.e., code t is a higher-fidelity refinement of code t' with no intermediate codes in between. Let $\mathcal{G} = (V, E)$ be the rooted DAG for this multi-fidelity simulation framework. We will discuss later how this “multi-fidelity DAG” can be elicited from a careful inspection of the scientific simulators.

Let $Z_t(\mathbf{x})$ be the simulation output at input \mathbf{x} from code t , $t \in V$. The GMGP assumes the following modeling framework:

$$\begin{cases} Z_t(\mathbf{x}) = \sum_{t' \in \text{Pa}(t)} \rho_{t'}(\mathbf{x}) Z_{t'}(\mathbf{x}) + \delta_t(\mathbf{x}), & t \in \overline{V_S}, \\ Z_{t'}(\mathbf{x}) \perp \delta_t(\mathbf{x}), & t' \in \text{Pa}(t). \end{cases} \quad (3)$$

Here, $V_S \subset V$ consists of all *source* nodes in \mathcal{G} (i.e., nodes with an in-degree of 0), $\overline{V_S} = V \setminus V_S$ contains the remaining nodes, and $\text{Pa}(t) = \{t' \in V : (t', t) \in E\}$ consists of all *parent* nodes of $t \in V$ in the DAG \mathcal{G} . Note that source nodes represent simulations with no lower-fidelity representations, and non-source nodes represent simulations with at least one lower-fidelity representation. We further assign the following GP priors on source nodes:

$$\begin{cases} Z_t(\mathbf{x}) \sim \mathcal{GP}(\mathbf{h}_t(\mathbf{x})^T \boldsymbol{\beta}_t, \sigma_t^2 r_t(\mathbf{x}, \mathbf{x}')), & t \in V_S \\ Z_t(\mathbf{x}) \perp Z_{t'}(\mathbf{x}), & t, t' \in V_S, \quad t \neq t'. \end{cases} \quad (4)$$

Here, $\mathbf{h}_t(\mathbf{x})$ is a vector of basis functions for the response surface mean at node t , with $\boldsymbol{\beta}_t$ its coefficients. For the discrepancy term $\delta_t(\mathbf{x})$, which captures the systematic difference between $Z_t(\mathbf{x})$ and its lower-fidelity representations, we assign independent GP priors:

$$\delta_t(\mathbf{x}) \sim \mathcal{GP}(\mathbf{h}_t(\mathbf{x})^T \boldsymbol{\beta}_t, \sigma_t^2 r_t(\mathbf{x}, \mathbf{x}')), \quad t \in \overline{V_S}. \quad (5)$$

Without prior information, the basis functions can be set as a constant mean, i.e., $\mathbf{h}_t(\mathbf{x}) \equiv 1$.

While the above specification may seem involved, the intuition is straight-forward.

For every non-source node $t \in \overline{V_S}$, its parent nodes $\text{Pa}(t)$ contain simulations which are lower-fidelity representations of code t . Equation (3) therefore presumes that, prior to data, $Z_t(\mathbf{x})$ can be decomposed as the weighted sum of its parent (lower-fidelity) codes, plus a discrepancy term $\delta_t(\mathbf{x})$ to model systematic bias. The key novelty over the KO model is that, instead of pooling information in a *sequence* from lowest to highest fidelity, the GMGP can integrate information over a more *general* DAG structure, which better captures model dependencies between simulations of complex systems. By leveraging this graphical dependency structure guided by the underlying scientific models, the GMGP can enjoy improved predictive performance over the KO model, as we show later.

The proposition below outlines two appealing modeling properties of the GMGP model:

Proposition 1. *The GMGP model defined above satisfies the following Markov properties:*

- (a) $Z_t(\mathbf{x}) \perp Z_{t'}(\mathbf{x}) | \{Z_j(\mathbf{x})\}_{j \in \text{Pa}(t)}$, for $t' \neq t$, $t' \notin \text{Des}(t)$, $t' \notin \text{Pa}(t)$,
- (b) $Z_t(\mathbf{x}) \perp Z_{t'}(\mathbf{x}') | \{Z_j(\mathbf{x})\}_{j \in \text{Pa}(t)}$, for $t' \in \text{Pa}(t)$, $\mathbf{x}' \neq \mathbf{x}$, if \mathcal{G} is a directed in-tree.

Here, $\text{Des}(t)$ denotes the set of descendant nodes for t , i.e., nodes t' for which there exists a path from t to t' .

The proof is provided in the Appendix, and the formal definition of a directed in-tree is provided and justified in the next section.

Property (a) states that, for a node t with input \mathbf{x} , its output $Z_t(\mathbf{x})$ and the output $Z_{t'}(\mathbf{x})$ at another node t' (where t' is a non-descendant, non-parent node of t) are conditionally independent, given the simulation output at the parent nodes $\{Z_j(\mathbf{x})\}_{j \in \text{Pa}(t)}$. In other words, given knowledge of the simulator at its immediate *lower-fidelity* (i.e., *parent*) nodes $\text{Pa}(t)$, the output at any simulator $Z_{t'}(\mathbf{x})$ which is not a *higher-fidelity refinement* (i.e., not a *descendant*) of t yields no additional information for predicting the simulator $Z_t(\mathbf{x})$ at node t . This is an intuitive modeling property if the edges in the DAG \mathcal{G} indeed represent

higher-fidelity refinements: at fixed input \mathbf{x} , simulations which are not higher-fidelity refinements of t should yield little (if any) additional information on t given its closest lower-fidelity representations. Property (a) can be viewed as an extension of the conditional independence property for Bayesian network models (Stephenson, 2000). Under a specific form for the multi-fidelity DAG \mathcal{G} (which we justify in the next section), Property (b) states that, conditioning on $\{Z_j(\mathbf{x})\}_{j \in \text{Pa}(t)}$, the simulation output $Z_t(\mathbf{x})$ is independent of the parent outputs $Z_{t'}(\mathbf{x}')$ at a different input \mathbf{x}' . In other words, given knowledge of the simulator at its immediate lower-fidelity (parent) nodes $\text{Pa}(t)$ with input \mathbf{x} , the output of such simulators at any other inputs \mathbf{x}' yields no additional information on predicting the output $Z_t(\mathbf{x})$ at node t . This can be viewed as an extension of the Markov property in O'Hagan (1998), which was used to justify the KO model.

The modeling framework (3)-(5) can then be used to derive the predictive distribution of the highest-fidelity code $Z_T(\mathbf{x})$. Suppose the parameters $\Theta = \{\beta_t, \sigma_t^2, \rho_t\}_{t=1}^T$ are fixed (these can be estimated via maximum likelihood or a fully Bayesian approach). Conditional on simulation data $\mathbf{z}^{(T)} = \{\mathbf{z}_1, \mathbf{z}_2, \dots, \mathbf{z}_T\}$, where $\mathbf{z}_t = \{Z_t(\mathbf{x}_i^t)\}_{i=1}^{n_t}$ are the observed outputs for simulator t , the predictive distribution for the highest-fidelity code at new input \mathbf{x} is given by:

$$[Z_T(\mathbf{x}) | \mathbf{z}^{(T)}, \Theta] \sim \mathcal{N}(\mu_{Z_T}(\mathbf{x}), \sigma_{Z_T}^2(\mathbf{x})),$$

where:

$$\begin{aligned} \mu_{Z_T}(\mathbf{x}) &= \left[\sum_{t' \in \text{Pa}(T)} \rho_{t'}(\mathbf{x}) \mathbf{h}_{t'}(\mathbf{x})^T \beta_{t'} + \mathbf{h}_T(\mathbf{x})^T \beta_T \right] + \mathbf{v}_T(\mathbf{x})^T \mathbf{V}_T^{-1} (\mathbf{z}^{(T)} - H_T \beta), \\ \sigma_{Z_T}^2(\mathbf{x}) &= v_{Z_T}^2(\mathbf{x}) - \mathbf{v}_T(\mathbf{x})^T \mathbf{V}_T^{-1} \mathbf{v}_T(\mathbf{x}). \end{aligned} \quad (6)$$

Here, $\mathbf{v}_T(\mathbf{x}) = \text{Cov}(Z_T(\mathbf{x}), \mathbf{z}^{(T)})$ is the covariance vector of the new observation $Z_T(\mathbf{x})$ and data $\mathbf{z}^{(T)}$, $\mathbf{V}_T = \text{Var}(\mathbf{z}^{(T)})$ is the covariance matrix of the data $\mathbf{z}^{(T)}$, $v_{Z_T}^2(\mathbf{x}) = \text{Var}(Z_T(\mathbf{x}))$

is the prior variance of the new observation $Z_T(\mathbf{x})$, H_T is the matrix of basis functions and $\boldsymbol{\beta} = \{\boldsymbol{\beta}_1, \dots, \boldsymbol{\beta}_T\}$ is the vector of coefficients such that $H_T\boldsymbol{\beta}$ yields the vector of prior means for $\mathbf{z}^{(T)}$ from (4).

While Equation (6) provides closed-form expressions for the predictive mean and variance, such expressions can be unwieldy to compute due to the inverse of the large matrix \mathbf{V}_T , which has dimensions $\sum_{t=1}^T n_t \times \sum_{t=1}^T n_t$. Motivated by Le Gratiet and Garnier (2014), we consider below a recursive formulation of the GMGP model which decouples this inverse over sub-graphs of the DAG, thus enabling scalable computation of the predictive distribution.

3.2 Recursive formulation

The key idea in this recursive reformulation is to *split* \mathcal{G} into separate sub-graphs, perform training and prediction on each sub-graph, then *combine* this information over the full graph \mathcal{G} to predict the highest-fidelity code. This is facilitated by the following model reformulation, which we later show yields the same predictive distribution as the GMGP model (3) under certain conditions:

$$\begin{cases} Z_t(\mathbf{x}) = \sum_{t' \in \text{Pa}(t)} \rho_{t'}(\mathbf{x}) Z_{t'}^*(\mathbf{x}) + \delta_t(\mathbf{x}), & t \in \overline{V_S} \\ Z_{t'}^*(\mathbf{x}) \perp \delta_t(\mathbf{x}), & t' \in \text{Pa}(t). \end{cases} \quad (7)$$

Here, $Z_{t'}^*(\cdot) = [Z_{t'}(\cdot) | \{\mathbf{z}_m\}_{m \in \text{Anc}(t')}, \mathbf{z}_{t'}]$ is the *posterior* distribution at node t' , conditional on data from both node t' and its ancestor nodes $\text{Anc}(t')$, i.e., nodes u such that there exists a path from u to t' . The same GP priors (5) are assigned for the discrepancy terms $\delta_t(\mathbf{x})$. The key difference between the recursive GMGP (or r-GMGP) model (7) and the GMGP model (3) is that, in place of $Z_{t'}(\mathbf{x})$ (the *prior* of the parent simulation) for the GMGP model, the r-GMGP model uses $Z_{t'}^*(\mathbf{x})$, the *posterior* of the parent simulation conditional on data.

Under (7), the posterior distribution of the highest-fidelity code Z_T can be shown to be

$$[Z_T(\mathbf{x})|\mathbf{z}^{(T)}, \Theta] \sim \mathcal{N}(m_{Z_T}(\mathbf{x}), s_{Z_T}^2(\mathbf{x})),$$

with the posterior mean and variance:

$$\begin{aligned} m_{Z_T}(\mathbf{x}) &= \sum_{t' \in \text{Pa}(T)} \rho_{t'}(\mathbf{x}) m_{Z_{t'}}(\mathbf{x}) + \mathbf{h}_T(\mathbf{x})^T \boldsymbol{\beta}_T \\ &\quad + \mathbf{r}_T(\mathbf{x}, \mathcal{D}_T)^T \mathbf{R}_T(\mathcal{D}_T)^{-1} \left[\mathbf{z}_T - \sum_{t' \in \text{Pa}(T)} \boldsymbol{\rho}_{t'}(\mathcal{D}_T) \odot \mathbf{z}_{t'}(\mathcal{D}_T) - \mathbf{h}_T(\mathcal{D}_T)^T \boldsymbol{\beta}_T \right], \quad (8) \\ s_{Z_T}^2(\mathbf{x}) &= \sum_{t' \in \text{Pa}(T)} \rho_{t'}^2(\mathbf{x}) s_{Z_{t'}}^2(\mathbf{x}) + \sigma_T^2 \left[1 - \mathbf{r}_T(\mathbf{x}, \mathcal{D}_T)^T \mathbf{R}_T(\mathcal{D}_T)^{-1} \mathbf{r}_T(\mathbf{x}, \mathcal{D}_T) \right]. \end{aligned}$$

Here, \odot denotes the Hadamard (entrywise) product, $\mathcal{D}_T = \{\mathbf{x}_i^T\}_{i=1}^{n_T}$ is the set of design points at node T , $\mathbf{r}_T(\mathbf{x}, \mathcal{D}_T)$ is the correlation vector between $Z_T(\mathbf{x})$ and \mathbf{z}_T , and $\mathbf{R}_T(\mathcal{D}_T)$ is the correlation matrix of \mathbf{z}_T . Equation (8) provides closed-form expressions for the predictive distribution of the highest-fidelity simulation T , which depend on only terms related to the current node T and its parent nodes $\text{Pa}(T)$. Indeed, (8) holds for all non-source nodes $t \in \overline{V_S}$, with closed-form expressions depending on only node t and its parent nodes $\text{Pa}(t)$. Thus, the desired predictive distribution $[Z_t(\mathbf{x})|\mathbf{z}^{(T)}, \Theta]$ can be efficiently evaluated, by *recursively* computing the posterior distribution using (8) on sub-graphs of \mathcal{G} , starting from its leaf nodes to its root. We show later that the predictive equations (8) for r-GMGP are precisely the desired predictive equations (6) for the GMGP model under certain conditions.

This recursive approach can yield significant computational savings over a naive evaluation of the original predictive equations (6), since it breaks up the inversion of the *large* covariance matrix \mathbf{V}_T into inversions of *smaller* matrices \mathbf{R}_t along each sub-graph. More precisely, with n_t denoting the sample size at node $t \in V$ and $n = \sum_{t \in V} n_t$ denoting the total sample size, this reduces the computational cost of $\mathcal{O}(n^3)$ for the original predictive

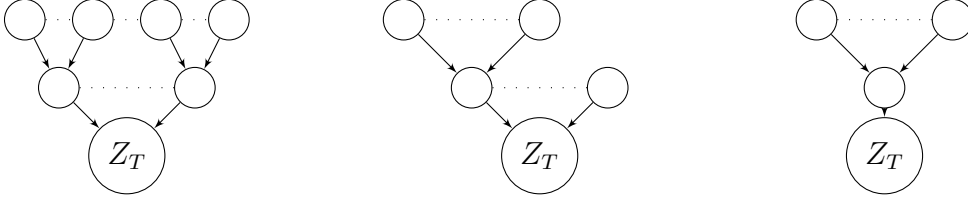


Figure 3: Examples of in-trees, with Z_T denoting the highest-fidelity simulator at the root.

equations (6) to a cost of $\mathcal{O}(T \max_t(n_t)^3)$ for the recursive approach in (8). Furthermore, if the inverse at each level of \mathcal{G} can be performed simultaneously via *distributed* computing, this computational cost can be further reduced to $\mathcal{O}(D \max_t(n_t)^3)$, where $D \leq T$ is the depth of the rooted graph \mathcal{G} . This shows that, when the sample sizes are moderately large at most nodes (which is typically the case for low-fidelity simulations), this recursive computation of the posterior predictive distribution over sub-graphs can yield large computational savings.

We now return to the important question of whether the r-GMGP predictive equations (8) are indeed the same as the predictive equations (6) for GMGP. To show this equivalence, we require a specific structure of the multi-fidelity DAG \mathcal{G} . Suppose \mathcal{G} is a directed *in-tree* (Mehlhorn and Sanders, 2008), defined as a rooted tree for which, at any node $t \in V$, there is exactly *one* path going from node t to the root node T (representing the highest-fidelity simulator Z_T). In-trees are also known as *anti-arborescence* trees (Korte and Vygen, 2011) in graph theory. Figure 3 shows several examples of directed in-trees. Under such an assumption on \mathcal{G} , the following proposition shows that the posterior predictive distribution for the highest-fidelity code Z_T is the same for the GMGP and r-GMGP models:

Proposition 2. *Suppose the rooted multi-fidelity DAG $\mathcal{G} = (V, E)$ is an in-tree. Further suppose (i) the observations are noise-free, and (ii) the design points are nested over \mathcal{G} , such that for any node $t \in V$, its design set \mathcal{D}_t is a subset of the designs at all parent nodes $\mathcal{D}_{t'}$, $t' \in \text{Pa}(t)$. Then the posterior predictive mean and variance from the GMGP and r-GMGP models are the same, i.e., $\mu_{Z_T}(\mathbf{x}) = m_{Z_T}(\mathbf{x})$ and $\sigma_{Z_T}^2(\mathbf{x}) = s_{Z_T}^2(\mathbf{x})$, where $\mu_{Z_T}(\mathbf{x})$ and $\sigma_{Z_T}^2(\mathbf{x})$ are the GMGP posterior mean and variance in (6), and $m_{Z_T}(\mathbf{x})$ and $s_{Z_T}^2(\mathbf{x})$*

are the *r*-GMGP posterior mean and variance in (8).

The proof of this proposition is provided in the Appendix. This proposition shows that the recursive GMGP model indeed yields the same predictive distribution as the original GMGP model when the multi-fidelity graph \mathcal{G} forms an in-tree, thus justifying the computational savings from r-GMGP. The assumption of \mathcal{G} being an in-tree implies that, for any simulator (i.e., node), there exists exactly one path in the employed simulation framework along which this model can be refined to the highest-fidelity simulator (i.e., root node). For example, the three heavy-ion collision models in the Introduction form a 3-node in-tree (see Figure 5a). In practice, such a property can often be satisfied via a careful *choice* of lower-fidelity simulators to run for training the multi-fidelity emulator. In cases where the simulators cannot be selected and do not form an in-tree, the original GMGP equations (6) may be used for prediction, albeit at higher computational cost.

For inference on model parameters, we employ a straight-forward extension of the maximum likelihood approach in Le Gratiet and Garnier (2014), which accounts for uncertainties in regression and correlation parameters within a universal co-kriging framework. Details on this approach can be found in Le Gratiet and Garnier (2014). In particular, our implementation of the r-GMGP model is built upon the R package `MuFiCokriging` (Le Gratiet, 2012) for this paper, which is available on CRAN.

4 Experimental Design

Given that the motivation behind the GMGP model is to maximize predictive performance given a computational budget, the *experimental design* of training runs is of crucial importance. This procedure can be split into two steps: (i) the *design* of training set \mathcal{D}_t at each node $t \in V$ given *fixed* sample sizes $n_t = |\mathcal{D}_t|$, and (ii) the *allocation* of sample sizes n_t at each node $t \in V$ given a *fixed* computational budget. We investigate these steps below.

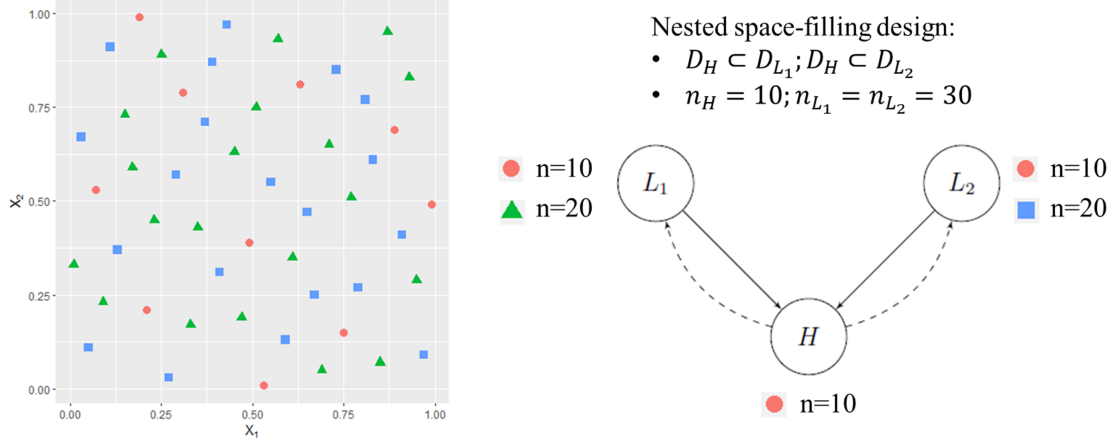


Figure 4: Visualizing the proposed nested BFS design for a 2-d design space. (Left) The base maximin SLHD design with 5 slices and 10 design points per slice. (Right) BFS allocation of the SLHD design over a three-node DAG. The first slice (red) is allocated to all three nodes, then subsequent slices (green and blue) are allocated to the lower-fidelity nodes L_1 and L_2 .

4.1 Design given fixed sample sizes

Consider first step (i). From Proposition 2, one appealing design property is the *nested* nature of design points over the graph \mathcal{G} , i.e., for any node $t \in V$, the design set \mathcal{D}_t is a subset of the designs $\mathcal{D}_{t'}$ at any parent node $t' \in \text{Pa}(t)$. Furthermore, for GP modeling, the *space-filling* property of design points (Santner et al., 2003) – its uniformity over the prediction space – is also known to be crucial for maximizing predictive performance. Different notions of space-fillingness have been explored in the literature, including maximin-type designs (Johnson et al., 1990; Morris and Mitchell, 1995; Joseph et al., 2015) and minimax-type designs (Johnson et al., 1990; Husslage et al., 2011; Mak and Joseph, 2018). We will incorporate these two properties in the following design procedure.

Given sample sizes n_1, \dots, n_T , we propose a nested experimental design over the DAG \mathcal{G} . We make use of the maximin sliced Latin hypercube design (maximin SLHD, Ba et al., 2015; see also Qian, 2012), which provides design points in equal *slices* (or batches), such that the design points *within* each slice are space-filling, and the design points *between* slices

Algorithm 1 Nested BFS Design

Input: DAG with $T = |V|$ nodes; desired sample sizes $\{n_t : t \in V\}$. Note that all n_t 's should be multiples of n_T .

Output: Design set \mathcal{D}_t for each node $t \in V$.

- 1: Generate a maximin SLHD design (Ba et al., 2015) with $M = \sum_{t=1}^T n_t/n_T$ slices, with each slice containing n_T design points.
 - 2: Assign the design points in slices $\{\sum_{j=1}^{t-1} n_j/n_T + 1, \dots, \sum_{j=1}^t n_j/n_T\}$ (denoted as S_t) to node t , $t = 1, \dots, T$.
 - 3: For each node t , set $\mathcal{D}_t = S_t \cup \{\cup_{t' \in \text{Des}(t)} S_{t'}\}$ for $t = 1, \dots, T$.
-

are also well spaced-out. Figure 4 (left) shows an SLHD in $d = 2$ dimensions. With this SLHD in hand, we then employ a *bottom-up* approach to allocate design points over \mathcal{G} . We first allocate one slice in the SLHD for the *highest-fidelity* simulator T (i.e., the root node at the bottom of \mathcal{G}), then use the remaining slices to fill out design points on subsequent nodes in a *breadth-first-traversal* (BFS, Cormen et al., 2009) of \mathcal{G} . For the latter step, the design points at each node $t \in V$ are obtained by concatenating the current SLHD slice(s) with design points on its descendant nodes $\text{Des}(t)$; this ensures the design is nested over the DAG \mathcal{G} . Figure 4 (right) visualizes this nested BFS design procedure. Intuitively, the use of maximin SLHDs allows one to “maximize” the information obtained over different nodes for predicting the high-fidelity response surface (we provide a more formal discussion of this in the next subsection). Algorithm 1 provides the detailed steps.

To implement this nested BFS design, however, there are certain conditions which need to hold for the sample sizes n_1, \dots, n_T . The first condition is that $n_{t'} \geq n_t$ if edge $(t', t) \in E$, i.e., a lower-fidelity node should always have as many sample points as its higher-fidelity counterpart. This is reasonable to expect in practice, since lower-fidelity simulations are by nature cheaper than higher-fidelity ones. The second condition is that the sample size n_t at any node t should be a multiple of the sample size n_T at the root (highest-fidelity) node. This allows us to evenly allocate slices of design points over each simulation node, thus maximizing the value from the sliced LHD structure. As we show later, this can be

satisfied by simply rounding off the sample sizes optimized in the following subsection.

4.2 Sample size allocation given fixed computational budget

Consider next step (ii), the allocation of sample sizes n_t given a fixed computational budget C . Let C_t denote the computational cost of performing a *single* run at simulation node $t \in V$, and let n_t be the allocated sample size at node $t \in V$. The budget constraint can then be written as $\sum_{t \in V} C_t n_t \leq C$.

We now derive a design criterion to minimize under this constraint for the sample sizes n_1, \dots, n_T . This follows from the proposition below (adapted from Wu and Schaback, 1993), which provides an upper bound on prediction error from the GMGP model. In what follows, we denote the response surface at source nodes by $\delta_t(\mathbf{x})$, $t \in V_S$.

Proposition 3. *Suppose the highest-fidelity code $Z_T(\mathbf{x})$ follows the recursive model (7). Further suppose that:*

1. *The parameter space Ω is bounded and convex,*
2. *The discrepancy term $\delta_t(\mathbf{x})$ is in the native space $N_{r_t}(\Omega)$ equipped with norm $\|\cdot\|_{N_{r_t}(\Omega)}$, where r_t is the correlation function in (5),*
3. *The correlation function r_t is the Matérn kernel with smoothness parameter ν .*

Then, using the posterior mean $m_{Z_T}(\mathbf{x})$ in (8), the prediction error can be upper bounded by:

$$|Z_T(\mathbf{x}) - m_{Z_T}(\mathbf{x})| \leq \sum_{t=1}^T \left(\prod_{t' \in \text{Des}(t) \cup \{t\} \setminus \{T\}} |\rho_{t'}(\mathbf{x})| \right) c_{r_t} h_{\mathcal{D}_t}^\nu \|\delta_t(\mathbf{x})\|_{N_{r_t}(\Omega)}. \quad (9)$$

Here, $h_{\mathcal{D}_t} = \max_{\mathbf{x} \in \Omega} \min_{i=1, \dots, n_t} \|\mathbf{x} - \mathbf{x}_i^t\|_2$ is the fill distance of design \mathcal{D}_t , and c_{r_t} is a constant depending on the length-scale parameters of r_t .

Our goal is then to find an optimal allocation of sample sizes n_1, \dots, n_T to minimize the error bound on the right side of (9), which in turn reduces the GMGP prediction error.

However, prior to data, we do not know what $\rho_t(\mathbf{x})$ and $\|\delta_t(\mathbf{x})\|_{N_{r_t}(\Omega)}$ are, and thus require further assumptions to evaluate the desired error bound. Suppose we make the simplifying assumptions that, *prior* to data, the correlation functions are constant over all nodes, i.e., $|\rho_t(\mathbf{x})| = \rho$, and that the native norm of the discrepancies are constant, i.e., $\|\delta_t(\mathbf{x})\|_{N_{r_t}(\Omega)} = \Delta$. Then, ignoring proportionality constants, the bound in (9) reduces to:

$$\sum_{t=1}^T \rho^{|\text{Des}(t)|} h_{\mathcal{D}_t}^\nu. \quad (10)$$

Additionally, if the design points \mathcal{D}_t at *each* node $t \in V$ are distributed in a manner which minimizes the fill distance asymptotically (this property is known as *low-dispersion*; see, e.g., Fang and Wang, 1993), then it is known that $h_{\mathcal{D}_t} = \mathcal{O}(n_t^{-1/d})$ (Wendland, 2004). This low-dispersion property is satisfied by most space-filling criteria in the literature (Pronzato, 2017). With this, the bound further simplifies to:

$$\sum_{t=1}^T \rho^{|\text{Des}(t)|} n_t^{-\nu/d} =: \Phi_\rho(n_1, \dots, n_T), \quad (11)$$

where $|\text{Des}(t)|$ is the number of descendant nodes on t . Consider now the minimization of the simplified bound $\Phi_\rho(n_1, \dots, n_T)$ given the budget constraint on sample sizes n_1, \dots, n_T :

$$\min_{n_1, \dots, n_T} \Phi_\rho(n_1, \dots, n_T) \quad \text{s.t.} \quad \sum_{t \in V} C_t n_t \leq C. \quad (12)$$

Using the method of Lagrange multipliers with Karush-Kuhn-Tucker conditions (Nocedal

and Wright, 2006), the optimal sample sizes can then be solved in closed-form as:

$$n_t \propto \left(\frac{\rho^{|\text{Des}(t)|}}{C_t} \right)^{d/(d+\nu)}, \quad \sum_{t \in V} C_t n_t = C. \quad (13)$$

Equation (13) provides a nice closed-form expression for sample size allocation over the multi-fidelity graph \mathcal{G} , where each node t has a different cost C_t per run. This yields two useful interpretations. First, nodes with higher costs per run are assigned smaller sample sizes by (13), which is intuitive since such experiments demand more computational resources. Second, assuming $\rho \in (0, 1)$, nodes with a greater number of descendant nodes (i.e., those with more higher-fidelity refinements) are assigned smaller sample sizes. This is also intuitive: such nodes are correlated and share information with its many descendant nodes, and thus require fewer samples compared to a node with few descendants.

To evaluate the optimal sample sizes in (13), however, we would need a prior estimate of the correlation parameter ρ . This may be obtained via a careful discussion with scientific modelers, to elicit the degree of correlation expected between simulation models prior to data. In the absence of such prior information, we suggest using a choice of ρ between 0.5 and 0.9, which allows for some integration of the underlying graphical structure for experimental design. The optimized samples sizes from (13) can then be used within the nested BFS design (Algorithm 1) to generate design points for multi-fidelity simulation. We show in Section 6 how this nested BFS design procedure with optimal sample size allocation can yield improved predictive performance for GMGP modeling.

5 The Deep GMGP Model

One potential limitation of the GMGP (and r-GMGP) model is that it presumes a linear correlation structure between simulation codes. Given enough training data, it may be

preferable to consider a more sophisticated emulator model which accounts for *nonlinear* correlations between nodes. We present next a “deep GMGP” (d-GMGP) model which incorporates this desired nonlinear structure via deep Gaussian processes (Damianou and Lawrence, 2013), inspired by the nonlinear autoregressive GPs in Perdikaris et al. (2017).

Similar to the r-GMGP model, let us assume the multi-fidelity DAG \mathcal{G} is a directed in-tree, with design points nested over \mathcal{G} . The d-GMGP model can be formulated as:

$$\begin{cases} Z_t(\mathbf{x}) = f_t(\{Z_{t'}(\mathbf{x}) : t' \in \text{Pa}(t)\} \cup \mathbf{x}) + \delta_t(\mathbf{x}), & t \in \overline{V_S} \\ f_t(\cdot) \perp \delta_t(\cdot). \end{cases} \quad (14)$$

Here, we again assign independent GP priors for the discrepancies $\delta_t(\mathbf{x}) \sim \mathcal{GP}(0, \sigma_t^2 r_t(\mathbf{x}, \mathbf{x}'))$, with similar independent GP priors on source nodes:

$$\begin{cases} Z_t(\mathbf{x}) \sim \mathcal{GP}(0, \sigma_t^2 r_t(\mathbf{x}, \mathbf{x}')), & t \in V_S \\ Z_t(\mathbf{x}) \perp Z_{t'}(\mathbf{x}), & t, t' \in V_S, \quad t \neq t'. \end{cases} \quad (15)$$

The key difference between the new model above and the GMGP model (3) is how the lower-fidelity (parent) nodes are integrated for higher-fidelity models. Instead of taking the weighted sum of the parent nodes $\sum_{t' \in \text{Pa}(t)} \rho_{t'}(\mathbf{x}) Z_{t'}(\mathbf{x})$, the d-GMGP model allows for a more *general* nonlinear transformation $f_t(\cdot)$ of the parent codes $\{Z_{t'}(\mathbf{x}) : t' \in \text{Pa}(t)\}$ as well the control parameters \mathbf{x} .

Since the transformation f_t is unknown in practice, one approach is to assign to it an independent zero-mean GP prior. For non-source nodes $t \in \overline{V_S}$, we can combine the GP priors on f_t and δ_t with Equation (14) to obtain the following general specification for $Z_t(\mathbf{x})$:

$$Z_t(\mathbf{x}) = g_t(\{Z_{t'}(\mathbf{x}) : t' \in \text{Pa}(t)\} \cup \mathbf{x}) \sim \mathcal{GP}(0, k_t([\mathbf{x}, \mathbf{z}], [\mathbf{x}', \mathbf{z}'])), \quad (16)$$

where $\mathbf{z} = \{Z_{t'}(\mathbf{x})\}_{t' \in \text{Pa}(t)}$ and $\mathbf{z}' = \{Z_{t'}(\mathbf{x}')\}_{t' \in \text{Pa}(t)}$. Note that the kernel k_t involves both the control parameters \mathbf{x} and the simulation outputs $Z_{t'}(\mathbf{x})$ from lower-fidelity (parent) nodes $t' \in \text{Pa}(t)$. Viewed this way, the proposed d-GMGP model can be seen as an extension of the deep GP model (see, e.g., Damianou and Lawrence, 2013), where the GP outputs at each node are linked by the multi-fidelity graphical structure elicited from model dependencies (i.e., the “science”). Compared to a full-blown deep GP model, which typically requires the estimation of thousands of variational parameters, the d-GMGP model (16) with the kernel choice below requires much fewer parameters for estimation, all the while providing the desired nonlinear correlations over the graph.

For the kernel k_t in (16), one specification we found quite effective is the following:

$$K_t([\mathbf{x}, \mathbf{z}], [\mathbf{x}', \mathbf{z}']) = K_{\text{SE}}(\mathbf{x}, \mathbf{x}') [K_{\text{LIN}}(\mathbf{z}, \mathbf{z}') + K_{\text{SE}}(\mathbf{z}, \mathbf{z}')] + K_{\text{SE}}(\mathbf{x}, \mathbf{x}'). \quad (17)$$

Here, $K_{\text{LIN}}(\cdot, \cdot) = \sigma^2 \mathbf{z}^T \mathbf{z}'$ is a linear kernel, σ^2 is a variance parameter, and $K_{\text{SE}}(\cdot, \cdot)$ is the anisotropic squared-exponential kernel. This is motivated by the kernel choice for the deep multi-fidelity GP models in Perdikaris et al. (2017) and Cutajar et al. (2019). The intuition behind (17) is that it captures both linear and nonlinear correlations between simulation outputs, as well as correlations between input parameters. In the case where $K_{\text{SE}}(\mathbf{z}, \mathbf{z}') = 0$, this kernel reduces to a form similar to the r-GMGP model, with $\rho(\mathbf{x})$ being modeled in a fully probabilistic and non-parametric form. In total, the specification in (17) requires $(1 + d)|V_S| + \sum_{t \in \overline{V_S}} (4 + 2d + |\text{Pa}(t)|)$ hyperparameters to estimate, which is again much fewer than that needed for a full-scale deep GP.

As before, a similar recursive formulation can be adopted for efficient fitting of the d-GMGP model. The idea is again to split the DAG \mathcal{G} into separate sub-graphs, then recursively train the model on each sub-graph. This is achieved by replacing the GP priors $Z_{t'}(\cdot)$, $t' \in \text{Pa}(t)$ in Equation (14) by the GP posteriors $Z_{t'}^*(\cdot) = [Z_{t'}(\cdot) | \{\mathbf{z}_m\}_{m \in \text{Anc}(t')}, \mathbf{z}_{t'}]$,

$t' \in \text{Pa}(t)$. With this, the desired posterior distribution on the highest-fidelity node $Z_T(\cdot)$ can be computed recursively on sub-graphs of \mathcal{G} , starting from its leaf nodes to its root, as was done for the r-GMGP model. Unlike the r-GMGP, however, the predictive distribution for the highest-fidelity node $Z_T(\cdot)$ is no longer Gaussian. This recursive formulation allows for efficient computation of the desired predictive distribution, by propagating the posterior uncertainty at each level using Monte Carlo. More specifically, the posterior distribution at a non-source node t can be evaluated by:

$$[Z_t^*(\mathbf{x})] = \int [Z_t(\mathbf{x})|\mathbf{z}_t, \mathbf{z}^*] \prod_{t' \in \text{Pa}(t)} [Z_{t'}^*(\mathbf{x})] d\mathbf{z}^*. \quad (18)$$

Here, \mathbf{z}_t are the observed data on node t , and $\mathbf{z}^* = \{Z_{t'}^*(\mathbf{x})\}_{t' \in \text{Pa}(t)}$ are the outputs on parent nodes at parameters \mathbf{x} which we marginalize over its posterior distribution. This can be estimated via Monte Carlo integration on the posterior distribution of parent nodes $[Z_{t'}^*(\mathbf{x})]$, $t' \in \text{Pa}(t)$. This procedure can then be repeated recursively over sub-graphs to provide efficient computation of the predictive distribution for the highest-fidelity node $Z_T(\cdot)$. Compared to full-scale deep GP model, this recursive approach provides a scalable way for propagating predictions and uncertainties to the root node, without the need for complex variational approximations. Algorithm 2 outlines the steps for d-GMGP prediction.

For the d-GMGP model, the computational cost for estimating hyperparameters using maximum likelihood is $\mathcal{O}(\sum_{t \in V} n_t^3)$, which is comparable to that for r-GMGP. Its prediction, however, is more time-consuming, as it requires *sampling* from the posterior distribution of each parent node model, then *propagating* these as inputs of each child node until we reach the root of the tree. Here, the posterior samples needed to achieve a desired accuracy for highest-fidelity prediction can grow exponentially with both the input dimensions and the size of the tree. One way to address this bottleneck is to employ a Gaussian approximation of the posterior predictive distribution at each node, then recursively compute the posterior

Algorithm 2 Computing the posterior predictive distribution for d-GMGP

Input: Training data $\{\mathcal{D}_t, \mathbf{z}_t\}$ over all nodes $t \in V$; Monte Carlo sample size N .

Output: Samples from the posterior predictive distribution for the highest-fidelity node $[Z_T(\mathbf{x})|\mathbf{z}^{(T)}]$.

```
1: Order the DAG nodes  $t = 1, \dots, T$  in terms of non-increasing depth (i.e., from leaf
   nodes to the root node).
2: For each node  $t = 1, \dots, T$ :
3:   If  $t \in V_S$  (i.e., if  $t$  is a source node):
4:     Fit a GP model on  $Z_t \sim \mathcal{GP}(0, \sigma_t^2 r_t(\mathbf{x}, \mathbf{x}'))$  using data  $\{\mathcal{D}_t, \mathbf{z}_t\}$ .
5:   Else:
6:     Compute the posterior means  $\mathbb{E}[Z_{t'}|\{\mathbf{z}_m\}_{m \in \text{Anc}(t')}, \mathbf{z}_{t'}]$  at design set  $\mathcal{D}_t$  for
       parent nodes  $t' \in \text{Pa}(t)$ .
7:     Fit a GP model (16) on  $Z_t$  with kernel (17).
8:   End If
9: End For
10: For each node  $t = 1, \dots, T$ :
11:   If  $t \in V_S$  (i.e., if  $t$  is a source node):
12:     Draw  $N$  samples  $\{z_{t,(i)}^*\}_{i=1}^N$  from the posterior distribution  $[Z_t(\mathbf{x})|\mathbf{z}_t]$ .
13:   Else:
14:     For  $i = 1, \dots, N$ , draw samples  $z_{t,(i)}^* \sim [Z_t(\mathbf{x})|\mathbf{z}_t, \{z_{t',(i)}^*\}_{t' \in \text{Pa}(t)}]$ .
15:   End If
16: End For
17: Return: Monte Carlo samples  $\{z_{T,(i)}^*\}_{i=1}^N$  from posterior distribution  $[Z_T(\mathbf{x})|\mathbf{z}^{(T)}]$ .
```

means and variances over the nodes in DAG \mathcal{G} . The latter step can be performed via the closed-form expressions in Girard et al. (2002) for GP predictions with uncertain inputs. Further details of this approximation can be found in Perdikaris et al. (2017).

6 Numerical Experiments

We now investigate the performance of the proposed GMGP models (r-GMGP and d-GMGP) compared to existing multi-fidelity models in a suite of numerical experiments. The following metrics are used for performance comparison:

- Root-mean-squared-error (RMSE): $\sqrt{M^{-1} \sum_{i=1}^M (\hat{y}_i - y_i)^2}$

- Probabilistic RMSE (p-RMSE): $\sqrt{M^{-1} \sum_{i=1}^M \mathbb{E}[(Y_i - y_i)^2 | \mathbf{z}^{(T)})]}$.

Here, y_i is the high-fidelity output for test point i ; \hat{y}_i is its prediction; Y_i is its posterior predictive distribution. RMSE measures the accuracy of the point prediction, whereas p-RMSE accounts for both bias and variance.

6.1 1-dimensional experiment

We first consider a simulation study using the simple 3-node graph in Figure 5a, with three correlated $d = 1$ -dimensional functions. The high-fidelity function (denoted H) is taken to be the Forrester function (Forrester et al., 2008) over the design space $[0, 1]$:

$$Z_H(x) = (6x - 2)^2 \sin(12x - 4),$$

and the two low-fidelity functions (L_1 and L_2) are derived from H as follows:

$$\begin{cases} Z_{L_1}(x) = \mathbb{1}_{\{x < 0.5\}} [Z_H(x) + (x - 0.5)] + \mathbb{1}_{\{x \geq 0.5\}} [Z_H(x) + (x - 0.5) \cos(40x)(5x - 1)^2] \\ Z_{L_2}(x) = \mathbb{1}_{\{x \leq 0.5\}} [Z_H(x) + 2(x - 0.5) \cos(10x)(10x - 1)^2] + \mathbb{1}_{\{x > 0.5\}} [Z_H(x) - (x - 0.5)] \end{cases}.$$

Figure 5b shows a visualization of the three test functions. Here, L_1 is designed to be closer to H on $[0, 0.5)$, while L_2 is closer to H on $(0.5, 1]$. This mimics a scenario where, due to simplifications in the underlying simulation model, low-fidelity functions might capture well the high-fidelity function in certain regions of the parameter space but not within other regions. The training sample sizes for L_1 , L_2 and H are set as 15, 15 and 8, respectively, with the design points in H nested within L_1 and L_2 . For testing, $M = 1000$ evenly-spaced points on $[0, 1]$ are used for performance comparison.

We compare 6 different predictive models here: the “high-fidelity” GP, two variants of the KO model, the NARGP model (Perdikaris et al., 2017), and the proposed r-GMGP

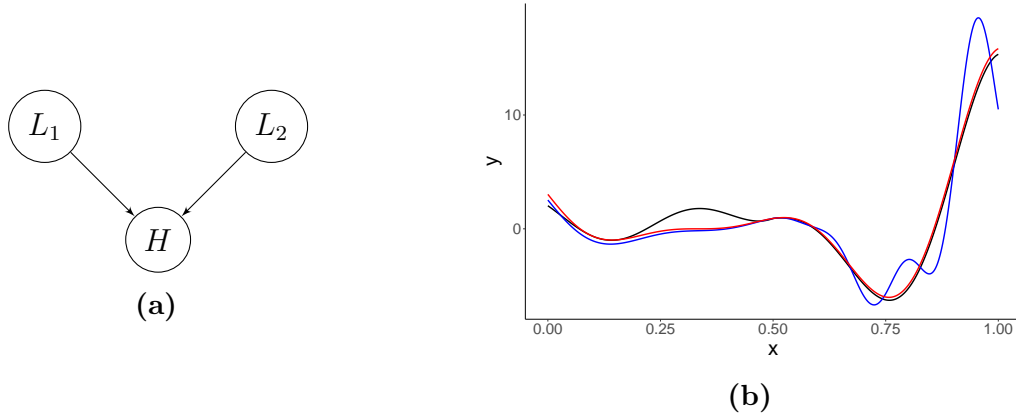


Figure 5: Visualizing the 1-d experiment: (a) the 3-node DAG used for generating the true functions; (b) the true high-fidelity (red), low-fidelity 1 (blue), and low-fidelity 2 (black) functions.

and d-GMGP models. For the high-fidelity GP, only the 8 points on H are used for model training. Recall that a key limitation of the KO model is that the simulations (see Figure 5a) cannot be ranked from lowest to highest fidelity. To that end, two variants of the KO model are considered. The first is the KO-path model (as discussed in Section 2.2), where the KO model is fit using only data along the longest path (here, $L_1 \rightarrow H$). The second is the KO-misspecified model, where the KO model is fit on the *full* simulation data with an arbitrary ordering from lowest to highest fidelity (here, $L_1 \rightarrow L_2 \rightarrow H$). Since the NARGP model also requires such a ranking, this model is fit on data from L_1 and H (similar to KO-path). Both the proposed r-GMGP and d-GMGP models make use of the full training dataset along with the implicit DAG structure for simulation. We apply the kernel in Perdikaris et al. (2017) for NARGP, kernel in (17) for d-GMGP, squared-exponential kernel for High-fidelity GP, and Matérn 5/2 kernel for others.

Figure 6 and Table 1 compare the predictive performance of the aforementioned predictive models. We see that the proposed r-GMGP and d-GMGP models yield noticeably improved predictions over existing models, in terms of both metrics. This improvement suggests that, when the underlying graphical model dependency structure is known from prior

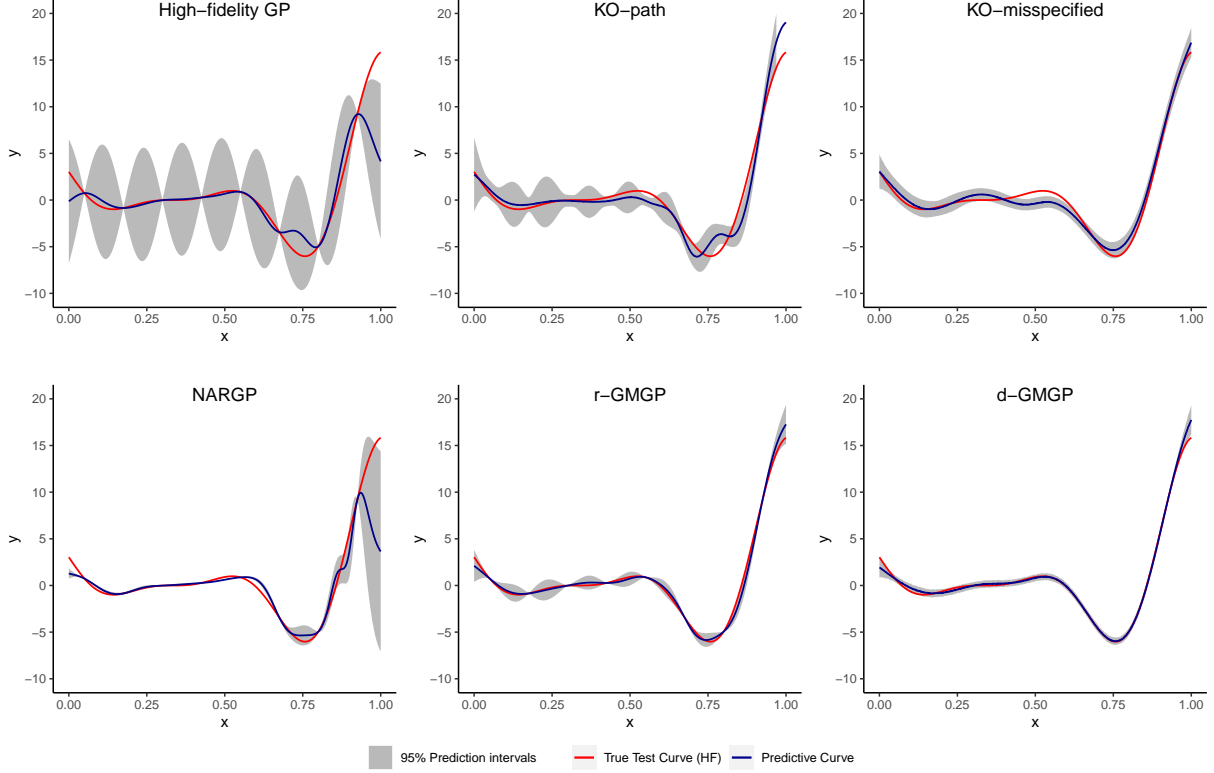


Figure 6: Results for the 1-d experiment: predictions (dark blue), 95% predictive intervals (gray), and the true high-fidelity function (red).

Model	1-d		5-d	
	RMSE	p-RMSE	RMSE	p-RMSE
High-fidelity GP	2.11	3.08	3.09	3.73
KO-path	1.07	1.38	1.41	1.54
KO-misspecified	0.61	0.76	0.63	0.85
NARGP	2.10	2.41	2.77	3.35
r-GMGP	0.39	0.53	0.70	0.99
d-GMGP	0.31	0.39	0.23	0.33

Table 1: Predictive metrics for the 1-d and 5-d experiments.

scientific knowledge, incorporating such structure can lead to better predictive performance. Comparing the two GMGP models, we see that the d-GMGP slightly outperforms the

r-GMGP. This is not too surprising, since from Figure 5b, we see that the correlations are quite nonlinear between the low and high fidelity functions, so a more flexible (nonlinear) correlation structure should yield improved predictive models.

6.2 5-dimensional experiment

Next, we compare the performance of the different methods on a $d = 5$ -dimensional experiment, with the same 3-node graph in Figure 5a. The high-fidelity function H (taken from Friedman (1991)) and the two low-fidelity functions L_1 and L_2 are given as follows:

$$\begin{cases} Z_H(\mathbf{x}) = 10 \sin(\pi x_1 x_2) + 20(x_3 - 0.5)^2 + 10x_4 + 5x_5 \\ Z_{L_1}(\mathbf{x}) = 10 \sin(4x_1 x_2) + 20(x_3 - 0.5)^2 + 10x_4 + 5(1.2x_5) \\ Z_{L_2}(\mathbf{x}) = 10 \sin(3x_1 x_2) + 20(0.8x_3 - 0.5)^2 + 10(x_4 - 0.1) + 5x_5 \end{cases}$$

The design points for L_1 , L_2 and H are generated from a sliced Latin Hypercube Design (SLHD, Ba et al., 2015) with sample sizes 40, 40 and 10, respectively, and the points in H are again nested within L_1 and L_2 . $M = 500$ random test samples are used for comparison.

Figure 7 and Table 1 show the predictive performance of the compared models. We see that, among the six plots in Figure 7, the predictive curve of the d-GMGP model is closest to the true test curve. Table 1 also shows that the proposed d-GMGP model indeed yields noticeably better predictive performance compared to other methods. This experiment again suggests that, when prior scientific information (in the form of a DAG) is available, integrating such information into a GP model can yield improved predictive performance. It is worth noting that the r-GMGP performs noticeably worse than the d-GMGP in this problem, and slightly worse than the KO-misspecified model. This is not unexpected, since again the true low and high-fidelity functions exhibit nonlinear correlations which are better captured by the d-GMGP model.

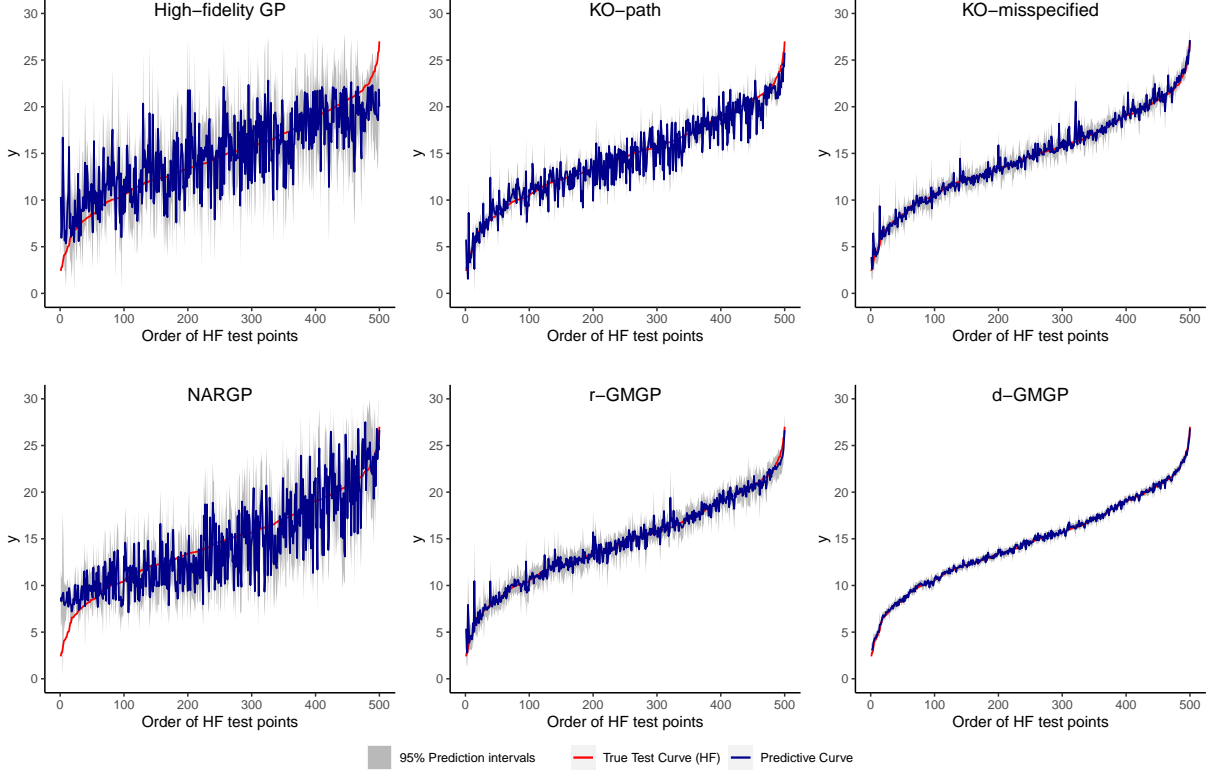


Figure 7: Results for the 5-d experiment: predictions (dark blue), 95% predictive intervals (gray) and the true high-fidelity function (red). Here, the points are ordered from lowest to highest according to the value of high-fidelity test output.

6.3 20-dimensional experiment

We then investigate the performance of GMGP models on a higher-dimensional problem with nonlinear correlation structures. We use here the 5-node DAG from Figure 2a, which consists of two low-fidelity functions (L_1 and L_2), two medium-fidelity functions (M_1 and M_2) and one high-fidelity function (H). The high-fidelity function H is taken to be the $d = 20$ -dimensional test function from Welch et al. (1992):

$$Z_H(\mathbf{x}) = \frac{5x_{12}}{1+x_1} + 5(x_4 - x_{20})^2 + x_5 + 40x_{19}^3 - 5x_{19} + 0.05x_2 + 0.08x_3 - 0.03x_6 + 0.03x_7 \\ - 0.09x_9 - 0.01x_{10} - 0.07x_{11} + 0.25x_{13}^2 - 0.04x_{14} + 0.06x_{15} - 0.01x_{17} - 0.03x_{18}$$

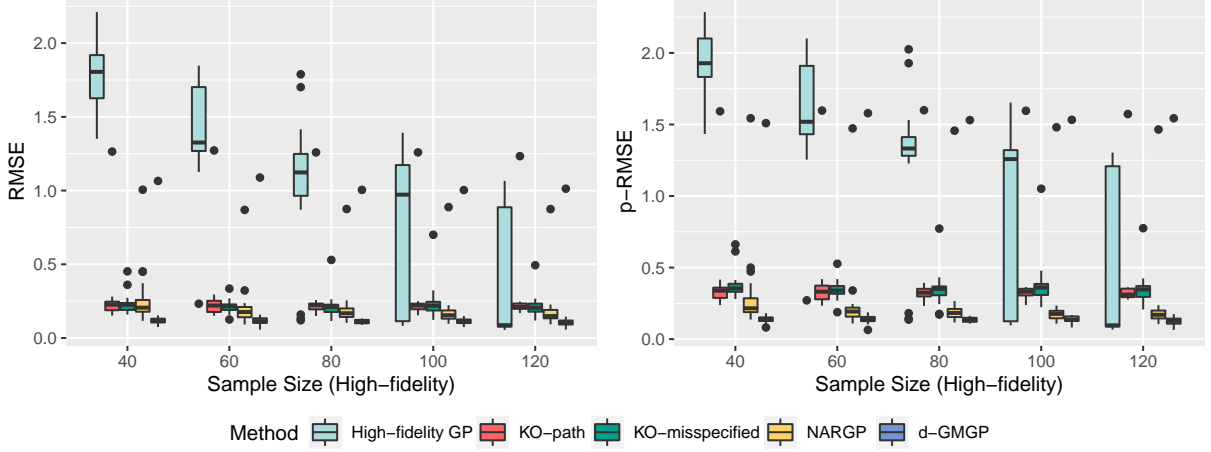


Figure 8: Results for the 20-d experiment: boxplots of two performance metrics for different sample sizes on H (left: RMSE, right: p-RMSE).

over design space $[-0.5, 0.5]^{20}$. The medium-fidelity function M_1 is obtained by *averaging* H over a sliding window of width $\pm 0.1x_l$ over each input $l = 1, \dots, 20$. The low-fidelity functions L_1 and L_2 are similarly obtained by averaging M_1 over a sliding window of size $\pm 0.15x_l$, over the 10 *odd* inputs (i.e., x_1, \dots, x_{19}) for L_1 , and over the 10 *even* inputs for L_2 . This mimics the scenario where lower-fidelity functions are obtained via some averaging operation, which is widely encountered in the physical sciences (e.g., fluid dynamics Pope, 2000). The remaining medium-fidelity function M_2 is obtained via a simple approximation of H : $Z_{M_2}(\mathbf{x}) = 1.2Z_H(\mathbf{x}) - 1$. Design points for L_1 , L_2 , M_1 , M_2 and H are again generated from a maximin SLHD with sample sizes set as 200, 200, 160, 160, and n_H , respectively, where the high-fidelity sample size n_H increases from 40 to 120 in increments of 20. For testing, $M = 500$ random test samples are used for comparison. This procedure is repeated for 20 times to account for error variability.

Figure 8 shows the error boxplots of the two metrics for various high-fidelity sample sizes. There are several observations of interest. First, for all sample sizes, the proposed d-GMGP model outperforms existing models, which again shows that, by leveraging the underlying model dependency structure in the form of a DAG, the proposed method can yield significant

improvements in terms of predictive performance. Second, this improvement seems to be most pronounced when the high-fidelity sample size is small. This is intuitive: as high-fidelity data become more limited and expensive, additional structure linking multi-fidelity data should be more effective in improving predictive performance. Here, the d-GMGP model seems quite capable of leveraging this DAG dependency structure for surrogate modeling, providing good predictive performance even in the challenging setting where high-fidelity data is limited in a high-dimensional input space.

6.4 Experimental design

Finally, we explore the effectiveness of the experimental design approach from Section 4 on the earlier 1-d and 5-d problems, which use the 3-node DAG in Figure 5a. For the 1-d problem, we set the computational cost per run at each node (L_1, L_2, H) to be $(2, 2, 32)$; for the 5-d problem, this cost per run is set as $(2, 2, 64)$, respectively. We then compare the design methods (discussed below) on cost budgets ranging from 160 to 360 in increments of 40 for the 1-d problem, and from 600 to 1200 in increments of 100 for the 5-d problem.

The proposed design from Section 4 is compared to two baseline design approaches given a fixed computational budget C . The first approach allocates the *full* budget to the high-fidelity node H . A Sobol' sequence (Joe and Kuo, 2003) is used for the 1-d problem, and a maximin LHD (Morris and Mitchell, 1995) is used for the 5-d problem. The second approach allocates the computational budget to the three nodes L_1 , L_2 and H with a *fixed* ratio of sample sizes. Two choices of fixed ratios are used: $6 : 6 : 1$ and $8 : 8 : 1$ for the 1-d problem, and $2 : 2 : 1$ and $3 : 3 : 1$ for the 5-d problem. The ratios are chosen such that the budget allocation is likely to be different from the proposed design. For the 1-d problem, a Sobol' sequence is used to generate the nested designs over the DAG (see Section 4.1 for details); for the 5-d problem, a maximin SLHD (Ba et al., 2015) is used to generate the nested designs. We then implement the proposed design approach with moderate correlation

($\rho = 0.5$ for 1-d, $\rho = 0.6$ for 5-d) and high correlation ($\rho = 0.9$), by first computing the desired sample size at each node via (13), then allocating the design points using the nested BFS design (Algorithm 1). The standard GP model and r-GMGP model with Matérn 5/2 kernel are then fit to the data, and the performances are compared via the RMSE of $M = 100$ test points for 1-d problem and $M = 500$ test points for 5-d problem. We repeat the procedure 20 times to reduce sampling variation.

Figure 9 shows the average RMSE of the compared design approaches for the 1-d and 5-d problems. We see that, given a fixed budget C , the proposed designs for both moderate and high correlations yield noticeably better predictive performance to both the high-fidelity design (where the full budget is allocated to high-fidelity runs) and the fixed ratio designs. This suggests that the proposed design approach, which jointly determines sample sizes and allocates sample points over each node in the DAG, is quite effective in reducing predictive error given a fixed budget, which is as desired. Furthermore, from these (and other) experiments, the performance of our designs appear quite robust to the choice of correlation parameter ρ , given it is sufficiently large (but not equal to 1). In applications where one expects a reasonable degree of correlation between simulation functions a priori, we would expect the proposed design with $\rho \in [0.5, 0.9]$ to yield better performance over a design with arbitrarily fixed ratio, and certainly over a design with only high-fidelity samples.

7 Multi-fidelity emulation of heavy-ion collisions

We now return to the motivating problem for multi-fidelity emulation of heavy-ion collisions. Experiments at Brookhaven National Laboratory and the European Organization for Nuclear Research (CERN) study collisions of atomic nuclei at velocities close to the speed of light. The temperature and pressure that the colliding nuclei are subjected to

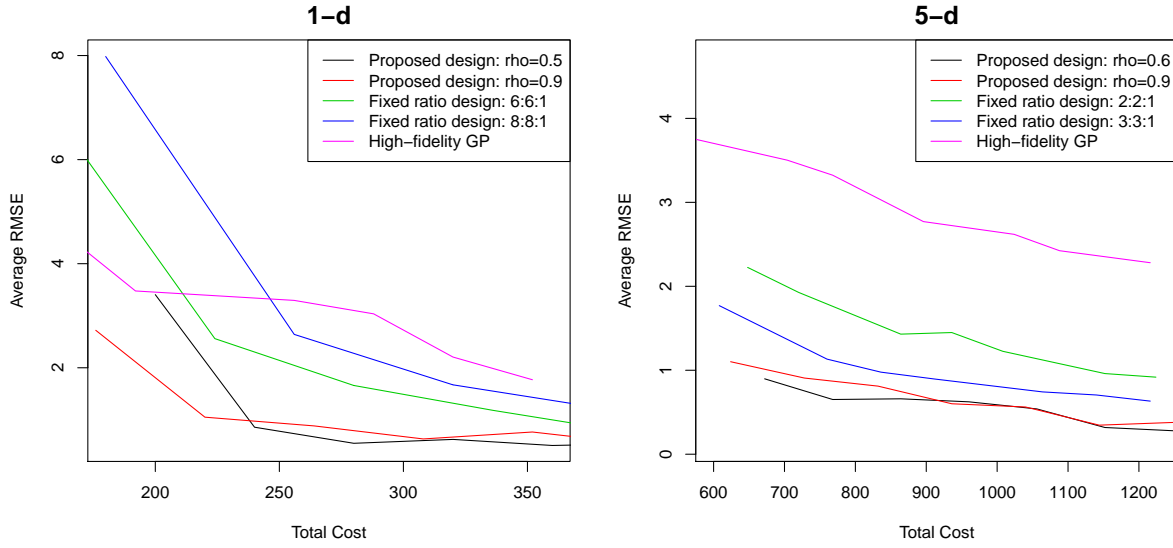


Figure 9: A comparison of average RMSE for five considered design procedures, for the 1-d problem (left) and the 5-d problem (right).

in these collisions converts them into a plasma of subatomic particles. However, *physical* experimentation of such collisions are very costly, requiring hundred millions of dollars in construction and operation. Because of this, the study of nuclear collisions has increasingly employed the use of *computer* simulations, which involve complex scientific models that describe successively different stages of the collision. Such computer experiments are then integrated with the limited physical experimental data for calibration of unknown physical parameters. In recent years, Bayesian inference with such multi-stage simulation models have led to novel discoveries on the properties of nuclear plasmas (Bernhard et al., 2019; Everett et al., 2021a,b). The computational cost of these simulations is considerable, however, requiring thousands of CPU hours per run over a high-dimensional parameter space. This presents a crucial bottleneck for a full-scale study of nuclear collisions, and emulator models are widely used to address this constraint (Novak et al., 2014; Bernhard et al., 2015, 2019; Everett et al., 2021b).

The computer models employed for simulating heavy-ion collisions naturally form a multi-stage model (Gale et al., 2013) as shown in Figure 1. In our study, we consider three broad stages. The first stage models the initial impact of the two nuclei prior to hydrodynamic evolution. This pre-hydrodynamic phase can be simulated by the computationally efficient Trento model (Moreland et al., 2015). The second stage involves the hydrodynamic evolution of the quark-gluon-plasma. A full-fledged simulation requires numerically expensive 3D hydrodynamic modeling (Jeon and Heinz, 2015) (which is too expensive for our study), so we neglect viscosity and consider “3+1D *ideal* QCD hydrodynamics” as the highest-fidelity model in this stage. This stage can be simplified by reducing the dimensionality of the hydrodynamic simulation from 3D to 1D, resulting in a lower-fidelity “1+1D ideal QCD hydrodynamics” model. A further simplification is the “1+1D linearized ideal conformal hydrodynamics” model, which replaces the equation of state of nuclear matter by a simpler conformal equation of state, and employs a linearization of the hydrodynamics equations. The third stage models the post-hydrodynamic conversion of the nuclear fluid into particles, using the Cooper-Frye prescription (Cooper and Frye, 1974). For the observables of interest in this study, it is possible to omit this conversion in lower fidelity models. The multi-stage simulation framework is visualized in Figure 1 and described in Everett et al. (2021b).

This multi-stage framework provides a rich testbed for multi-fidelity simulations, since experiments of different fidelities can be performed via different model combinations at each stage. After close discussions, we decided to run the following three models:

- L_1 : Pre-hydrodynamics + linearized ideal conformal hydrodynamics + Cooper-Frye,
- L_2 : Pre-hydrodynamics + 1+1D ideal QCD hydrodynamics,
- H : Pre-hydrodynamics + 3+1D ideal QCD hydrodynamics + Cooper-Frye.

From the earlier description, it follows that H is the highest-fidelity model, and L_1 and L_2 can be viewed as lower-fidelity representations of H . The corresponding DAG for this

Parameter	Description	Range
x_1	nucleon width	$[0.35, 1.40](\text{fm})$
x_2	constituent width fraction	$[0.1, 0.9]$
x_3	minimum transverse kinematic cut	$[0.2, 1.0](\text{GeV})$
x_4	fragment profile shape α	$[3.0, 5.0]$
x_5	fragment profile shape β	$[-1.0, 0.0]$
x_6	midrapidity energy density power	$[0.30, 0.48]$
x_7	midrapidity energy density normalization	$[0.20, 0.45]$
x_8	fireball–fragment fluctuation	$[0.1, 0.6]$
x_9	fireball profile shape	$[1.0, 1.5]$

Table 2: *Description and range of the $d = 9$ input parameters for the heavy-ion collision simulator.*

simulation is provided in Figure 5a.

Table 2 summarizes the $d = 9$ input parameters in this computer experiment, which are shared by all three simulation models. Here, we study a single output (or “observable”), which is the ratio of pions produced at rapidity $y = 0$ and rapidity $y = 1$.¹ To train the emulator model, we first simulate 25, 200 and 200 training points from the models H , L_1 and L_2 , respectively. These design points are obtained via a maximin SLHD design (Ba et al., 2015), such that the design for H is nested within that for L_1 and L_2 (see Section 4.1 for details). To evaluate predictive performance, $M = 75$ out-of-sample testing points are generated from a maximin LHD design. As before, we compare the proposed d-GMGP model (which yielded the best predictive performance from simulations) with the high-fidelity GP, the two variants of the KO model (KO-path and KO-misspecified), and the NARGP model in Perdikaris et al. (2017).

Table 3 reports the predictive performance metrics for the considered emulator models. We see that, among all five models, the proposed d-GMGP gives the best predictive performance, providing noticeable reductions over both test error metrics. This again

¹In the L_2 model, which does not include a particlization step, we instead compute the ratio of entropy densities, treating them as proxies for pion production to within a common proportionality factor.

Model	Metrics ($\times 10^{-2}$)	
	RMSE	p-RMSE
High-fidelity GP	5.49	5.83
KO-path	3.48	3.80
KO-misspecified	3.95	4.45
NARGP	3.66	3.83
d-GMGP	2.17	2.44

Table 3: *Predictive performance metrics for the considered models in the heavy-ion collision emulation problem.*

suggests that, by integrating the DAG dependency structure between the simulators (i.e., the “science”) as prior knowledge, one can greatly improve the predictive performance of the resulting multi-fidelity emulator. This “science” appears to play a key role: compared to the KO-misspecified model, which misspecifies the underlying scientific connections between simulation models, the proposed GMGP model yields noticeable improvements in predictive performance by integrating model dependency information elicited from a careful inspection of the modeled physics. This can then be used for improved parameter constraints on nuclear plasma properties, leading to more precise scientific discoveries given a fixed computational budget.

8 Conclusion

We proposed in this paper a new Graphical Multi-fidelity Gaussian Process (GMGP) model for multi-fidelity predictive modeling. The key novelty of the GMGP model is the integration of scientific information in the form of a DAG, which captures connections between different simulation models in terms of fidelities. This DAG should be obtained via a careful inspection of the scientific simulation models and discussion with domain scientists. We show that the GMGP model has appealing properties for multi-fidelity

modeling, and present two extensions which allow for nonlinear modeling and scalable prediction via recursive computation of the posterior predictive distribution on sub-graphs. We also present a comprehensive experimental design methodology for the GMGP, which jointly determines the sample size on each simulation model and its corresponding design points over the parameter space. Extensive numerical experiments and an application in heavy-ion collisions demonstrate the improvement of the proposed method over existing multi-fidelity models, particularly given a tight computational budget for simulations.

There are several interesting avenues for future work. One limitation of the current framework is that the equivalence of GMGP and r-GMGP is only shown for when the multi-fidelity graph \mathcal{G} forms a directed in-tree. Although this assumption can often be satisfied via a careful design of the lower-fidelity models, it may be violated for problems where the multi-fidelity training data is *observed* rather than designed. It would therefore be of interest to extend the recursive formulation of the GMGP for more general graphs in such problems. Furthermore, to avoid computationally expensive numerical integration steps, the GMGP model currently does not account for uncertainties in variance parameters and lengthscales. Another intriguing future direction would be to explore an efficient fully Bayesian implementation of the GMGP model which accounts for uncertainties from all model parameters. The recent work of Ma (2020) seems to be promising for this direction. Finally, it may be of interest to extend the GMGP model for noisy data, which may arise in the case of noisy simulators (Ankenman et al., 2008).

9 Acknowledgements

This work was supported by the U.S. Department of Energy grant DE-FG02-05ER41367 (SAB, JFP and DS) as well as by NSF grant OAC-1550225 (YJ, DS and SM).

References

- Ankenman, B., Nelson, B. L., and Staum, J. (2008). Stochastic kriging for simulation metamodeling. In *2008 Winter Simulation Conference*, pages 362–370. IEEE.
- Ba, S., Myers, W. R., and Brenneman, W. A. (2015). Optimal sliced Latin hypercube designs. *Technometrics*, 57(4):479–487.
- Bernhard, J. E., Marcy, P. W., Coleman-Smith, C. E., Huzurbazar, S., Wolpert, R. L., and Bass, S. A. (2015). Quantifying properties of hot and dense QCD matter through systematic model-to-data comparison. *Physical Review C*, 91(5):054910.
- Bernhard, J. E., Moreland, J. S., and Bass, S. A. (2019). Bayesian estimation of the specific shear and bulk viscosity of quark–gluon plasma. *Nature Physics*, 15(11):1113–1117.
- Chen, J., Mak, S., Joseph, V. R., and Zhang, C. (2021). Function-on-function kriging, with applications to three-dimensional printing of aortic tissues. *Technometrics*, 63(3):384–395.
- Cooper, F. and Frye, G. (1974). Single-particle distribution in the hydrodynamic and statistical thermodynamic models of multiparticle production. *Physical Review D*, 10(1):186.
- Cormen, T. H., Leiserson, C. E., Rivest, R. L., and Stein, C. (2009). *Introduction to Algorithms*. MIT press.
- Cutajar, K., Pullin, M., Damianou, A., Lawrence, N., and González, J. (2019). Deep Gaussian processes for multi-fidelity modeling. *arXiv preprint arXiv:1903.07320*.
- Damianou, A. and Lawrence, N. D. (2013). Deep Gaussian processes. In *Artificial Intelligence and Statistics*, pages 207–215. PMLR.
- Ding, L., Mak, S., and Wu, C. F. J. (2019). BdryGP: a new Gaussian process model for incorporating boundary information. *arXiv preprint arXiv:1908.08868*.
- Everett, D., Ke, W., Paquet, J.-F., Vujanovic, G., Bass, S., Du, L., Gale, C., Heffernan, M., Heinz, U., Liyanage, D., et al. (2021a). Phenomenological constraints on the transport properties of QCD matter with data-driven model averaging. *Physical Review Letters*, 126(24):242301.
- Everett, D., Ke, W., Paquet, J.-F., Vujanovic, G., Bass, S. A., Du, L., Gale, C., Heffernan, M., Heinz, U., Liyanage, D., et al. (2021b). Multisystem Bayesian constraints on the transport coefficients of QCD matter. *Physical Review C*, 103(5):054904.
- Fang, K.-T. and Wang, Y. (1993). *Number-theoretic Methods in Statistics*, volume 51. CRC Press.
- Fernández-Godino, M. G., Park, C., Kim, N.-H., and Haftka, R. T. (2016). Review of multi-fidelity models. *arXiv preprint arXiv:1609.07196*.
- Forrester, A., Sobester, A., and Keane, A. (2008). *Engineering Design via Surrogate Modelling: A Practical Guide*. John Wiley & Sons.
- Friedman, J. H. (1991). Multivariate adaptive regression splines. *The Annals of Statistics*, pages 1–67.
- Gale, C., Jeon, S., and Schenke, B. (2013). Hydrodynamic modeling of heavy-ion collisions. *International Journal of Modern Physics A*, 28:1340011.

- Girard, A., Rasmussen, C. E., Quinonero-Candela, J., and Murray-Smith, R. (2002). Gaussian process priors with uncertain inputs - application to multiple-step ahead time series forecasting. *Advances in Neural Information Processing Systems*, 15:545–552.
- Golchi, S., Bingham, D. R., Chipman, H., and Campbell, D. A. (2015). Monotone emulation of computer experiments. *SIAM/ASA Journal on Uncertainty Quantification*, 3(1):370–392.
- Gorodetsky, A. A., Jakeman, J. D., and Geraci, G. (2020a). MFNets: learning network representations for multifidelity surrogate modeling. *arXiv preprint arXiv:2008.02672*.
- Gorodetsky, A. A., Jakeman, J. D., Geraci, G., and Eldred, M. S. (2020b). MFNets: multi-fidelity data-driven networks for Bayesian learning and prediction. *International Journal for Uncertainty Quantification*, 10(6).
- Hung, Y., Joseph, V. R., and Melkote, S. N. (2015). Analysis of computer experiments with functional response. *Technometrics*, 57(1):35–44.
- Husslage, B. G. M., Rennen, G., van Dam, E. R., and den Hertog, D. (2011). Space-filling Latin hypercube designs for computer experiments. *Optimization and Engineering*, 12(4):611–630.
- Jeon, S. and Heinz, U. (2015). Introduction to hydrodynamics. *International Journal of Modern Physics E*, 24(10):1530010.
- Joe, S. and Kuo, F. Y. (2003). Remark on algorithm 659: Implementing Sobol’s quasirandom sequence generator. *ACM Transactions on Mathematical Software (TOMS)*, 29(1):49–57.
- Johnson, M. E., Moore, L. M., and Ylvisaker, D. (1990). Minimax and maximin distance designs. *Journal of Statistical Planning and Inference*, 26(2):131–148.
- Joseph, V. R., Gul, E., and Ba, S. (2015). Maximum projection designs for computer experiments. *Biometrika*, 102(2):371–380.
- Kaufman, C. G., Bingham, D., Habib, S., Heitmann, K., and Frieman, J. A. (2011). Efficient emulators of computer experiments using compactly supported correlation functions, with an application to cosmology. *The Annals of Applied Statistics*, 5(4):2470–2492.
- Kennedy, M. C. and O’Hagan, A. (2000). Predicting the output from a complex computer code when fast approximations are available. *Biometrika*, 87(1):1–13.
- Korte, B. H. and Vygen, J. (2011). *Combinatorial Optimization*, volume 1. Springer.
- Le Gratiet, L. (2012). *MuFiCokriging: multi-fidelity cokriging models*. R package version 1.2.
- Le Gratiet, L. (2013). Bayesian analysis of hierarchical multifidelity codes. *SIAM/ASA Journal on Uncertainty Quantification*, 1(1):244–269.
- Le Gratiet, L. and Garnier, J. (2014). Recursive co-kriging model for design of computer experiments with multiple levels of fidelity. *International Journal for Uncertainty Quantification*, 4(5):365–386.
- López-Lopera, A. F., Bartoli, N., Lefèvre, T., and Mouton, S. (2021). Data fusion with multi-fidelity Gaussian processes for aerodynamic experimental and numerical databases. In *SIAM Conference on Computational Science and Engineering (CSE)*.

- Ma, P. (2020). Objective Bayesian analysis of a cokriging model for hierarchical multifidelity codes. *SIAM/ASA Journal on Uncertainty Quantification*, 8(4):1358–1382.
- Mak, S. and Joseph, V. R. (2018). Minimax and minimax projection designs using clustering. *Journal of Computational and Graphical Statistics*, 27(1):166–178.
- Mak, S., Sung, C.-L., Wang, X., Yeh, S.-T., Chang, Y.-H., Joseph, V. R., Yang, V., and Wu, C. F. J. (2018). An efficient surrogate model for emulation and physics extraction of large eddy simulations. *Journal of the American Statistical Association*, 113(524):1443–1456.
- Mehlhorn, K. and Sanders, P. (2008). *Algorithms and Data Structures: The Basic Toolbox*, volume 55. Springer.
- Moreland, J. S., Bernhard, J. E., and Bass, S. A. (2015). Alternative ansatz to wounded nucleon and binary collision scaling in high-energy nuclear collisions. *Physical Review C*, 92(1):011901.
- Morris, M. D. and Mitchell, T. J. (1995). Exploratory designs for computational experiments. *Journal of Statistical Planning and Inference*, 43(3):381–402.
- Nocedal, J. and Wright, S. (2006). *Numerical Optimization*. Springer Science & Business Media.
- Novak, J., Novak, K., Pratt, S., Vredevogd, J., Coleman-Smith, C., and Wolpert, R. (2014). Determining fundamental properties of matter created in ultrarelativistic heavy-ion collisions. *Physical Review C*, 89(3):034917.
- O’Hagan, A. (1998). A Markov property for covariance structures. Technical report, University of Nottingham.
- Peherstorfer, B., Willcox, K., and Gunzburger, M. (2018). Survey of multifidelity methods in uncertainty propagation, inference, and optimization. *SIAM Review*, 60(3):550–591.
- Perdikaris, P., Raissi, M., Damianou, A., Lawrence, N. D., and Karniadakis, G. E. (2017). Nonlinear information fusion algorithms for data-efficient multi-fidelity modelling. *Proceedings of the Royal Society A: Mathematical, Physical and Engineering Sciences*, 473(2198):20160751.
- Pilania, G., Gubernatis, J. E., and Lookman, T. (2017). Multi-fidelity machine learning models for accurate bandgap predictions of solids. *Computational Materials Science*, 129:156–163.
- Pope, S. B. (2000). *Turbulent Flows*. Cambridge university press.
- Pronzato, L. (2017). Minimax and maximin space-filling designs: some properties and methods for construction. *Journal de la Société Française de Statistique*, 158(1):7–36.
- Qian, P. Z. G. (2012). Sliced Latin hypercube designs. *Journal of the American Statistical Association*, 107(497):393–399.
- Qian, P. Z. G. and Wu, C. F. J. (2008). Bayesian hierarchical modeling for integrating low-accuracy and high-accuracy experiments. *Technometrics*, 50(2):192–204.
- Russell, S. and Norvig, P. (2003). *Artificial Intelligence: A Modern Approach*. Prentice Hall, second edition.
- Santner, T. J., Williams, B. J., and Notz, W. I. (2003). *The Design and Analysis of*

- Computer Experiments*, volume 1. Springer.
- Stephenson, T. A. (2000). An introduction to Bayesian network theory and usage. Technical report, IDIAP.
- Wang, X. and Berger, J. O. (2016). Estimating shape constrained functions using Gaussian processes. *SIAM/ASA Journal on Uncertainty Quantification*, 4(1):1–25.
- Welch, W. J., Buck, R. J., Sacks, J., Wynn, H. P., Mitchell, T. J., and Morris, M. D. (1992). Screening, predicting, and computer experiments. *Technometrics*, 34(1):15–25.
- Wendland, H. (2004). *Scattered Data Approximation*, volume 17. Cambridge University Press.
- Wu, Z. and Schaback, R. (1993). Local error estimates for radial basis function interpolation of scattered data. *IMA Journal of Numerical Analysis*, 13(1):13–27.
- Zhang, R., Mak, S., and Dunson, D. (2021). Gaussian process subspace regression for model reduction. *arXiv preprint arXiv:2107.04668*.

A Proof of Proposition 1

A.1 Property (a)

Property (a) can be derived from the well-known Factorization Theorem for Bayesian networks (Russell and Norvig, 2003). By assuming a Bayesian Network structure over the DAG, the joint distribution of observations at all nodes can be factorized as

$$P(X_1, X_2, \dots, X_n) = \prod_{i=1}^n P(X_i | \{X_j\}_{j \in \text{Pa}(i)}).$$

Then, for all X_t , we have:

$$\begin{aligned} P(X_t | \{X_j\}_{j \in \text{Anc}(t)}) &= \frac{P(X_t, \{X_j\}_{j \in \text{Anc}(t)})}{P(\{X_j\}_{j \in \text{Anc}(t)})} \\ &= \frac{\prod_{l \in \text{Anc}(t) \cup \{t\}} P(X_l | \{X_m\}_{m \in \text{Pa}(l)})}{\prod_{l \in \text{Anc}(t)} P(X_l | \{X_m\}_{m \in \text{Pa}(l)})} \\ &= P(X_t | \{X_j\}_{j \in \text{Pa}(t)}). \end{aligned}$$

Thus, conditioning on parent nodes of t , it follows that X_t and ancestors of t that are not parent nodes are independent, i.e., $Z_t(\mathbf{x}) \perp Z_{t'}(\mathbf{x}) | \{Z_j(\mathbf{x})\}_{j \in \text{Pa}(t)}$ for all $t' \neq t, t' \notin \text{Des}(t), t' \notin \text{Pa}(t)$.

A.2 Property (b)

Next, we present the proof of Property (b) for the simplest 3-node in-tree (Figure 10). This approach can be extended analogously for more complicated in-trees.

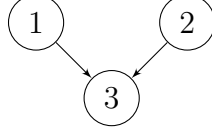


Figure 10: *Simplest 3-node in-tree.*

Proof. The GMGP model for a 3-node in-tree is given as follows:

$$\begin{cases} Z_3(\mathbf{x}) = \rho_1(\mathbf{x}) \cdot Z_1(\mathbf{x}) + \rho_2(\mathbf{x}) \cdot Z_2(\mathbf{x}) + \delta_3(\mathbf{x}) \\ \delta_3(\mathbf{x}) \perp Z_1(\mathbf{x}), \delta_3(\mathbf{x}) \perp Z_2(\mathbf{x}), Z_1(\mathbf{x}) \perp Z_2(\mathbf{x}). \end{cases}$$

Thus we have for $\mathbf{x}' \neq \mathbf{x}$,

$$\text{Cov}(Z_3(\mathbf{x}), Z_1(\mathbf{x}')) = \text{Cov}(\rho_1(\mathbf{x}) \cdot Z_1(\mathbf{x}), Z_1(\mathbf{x}')) = \rho_1(\mathbf{x}) \cdot \text{Cov}(Z_1(\mathbf{x}), Z_1(\mathbf{x}')),$$

and

$$\begin{aligned} & [\text{Cov}(Z_3(\mathbf{x}), Z_1(\mathbf{x})), \text{Cov}(Z_3(\mathbf{x}), Z_2(\mathbf{x}))] \begin{bmatrix} \text{Var}(Z_1(\mathbf{x}))^{-1} & 0 \\ 0 & \text{Var}(Z_2(\mathbf{x}))^{-1} \end{bmatrix} \begin{bmatrix} \text{Cov}(Z_1(\mathbf{x}'), Z_1(\mathbf{x})) \\ \text{Cov}(Z_1(\mathbf{x}'), Z_2(\mathbf{x})) \end{bmatrix} \\ &= \text{Cov}(Z_3(\mathbf{x}), Z_1(\mathbf{x})) \text{Var}(Z_1(\mathbf{x}))^{-1} \text{Cov}(Z_1(\mathbf{x}), Z_1(\mathbf{x}')) + \text{Cov}(Z_3(\mathbf{x}), Z_2(\mathbf{x})) \text{Var}(Z_2(\mathbf{x}))^{-1} \text{Cov}(Z_2(\mathbf{x}), Z_1(\mathbf{x}')) \\ &= \rho_1(\mathbf{x}) \cdot \text{Var}(Z_1(\mathbf{x})) \text{Var}(Z_1(\mathbf{x}))^{-1} \text{Cov}(Z_1(\mathbf{x}), Z_1(\mathbf{x}')) + 0 \\ &= \rho_1(\mathbf{x}) \cdot \text{Cov}(Z_1(\mathbf{x}), Z_1(\mathbf{x}')). \end{aligned}$$

From the above two expressions, we have

$$\begin{aligned} & \text{Cov}(Z_3(\mathbf{x}), Z_1(\mathbf{x}') | Z_1(\mathbf{x}), Z_2(\mathbf{x})) \\ &= \rho_1(\mathbf{x}) \cdot \text{Cov}(Z_1(\mathbf{x}), Z_1(\mathbf{x}')) - \rho_1(\mathbf{x}) \cdot \text{Cov}(Z_1(\mathbf{x}), Z_1(\mathbf{x}')) \\ &= 0. \end{aligned}$$

Similarly, we can show that $\text{Cov}(Z_3(\mathbf{x}), Z_2(\mathbf{x}') | Z_1(\mathbf{x}), Z_2(\mathbf{x})) = 0$, $\mathbf{x}' \neq \mathbf{x}$. This approach can be naturally extended for general in-trees, and thus Property (b) in Proposition 1 then follows.

B Proof of Proposition 2

We adopt an inductive approach to prove Proposition 2. In Subsection B.1 we first show that the equivalence between the GMGP and r-GMGP model for the simplest 3-node in-tree of depth 2 (see Figure 10), and argue that this naturally extends for in-trees of depth 2 with more than two branches (see Figure 11). This establishes the base case for induction. In Subsection B.2, we then show this equivalence for in-trees constructed by connecting two lower-level in-trees to a root node (see Figure 12a), and again argue that this extends for in-trees connected by more lower-level in-trees (see Figure 12b). This provides the inductive step. Finally, to complete the proof, we leverage the fact that any directed in-trees can be recursively constructed via the construction in Figure 12b, thus proving the equivalence between the GMGP and r-GMGP for all directed in-trees.

B.1 Sub-graphs starting with source nodes

Proof. Let us again consider the simplest 3-node in-tree, as shown in Figure 10. We extend the proof in Le Gratiet and Garnier (2014) as follows. Note that the proof below naturally generalizes to the case of in-trees with multiple source nodes (see Figure 11).

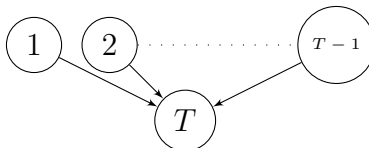


Figure 11: *In-trees of depth 2 with multiple source nodes.*

Let \mathcal{D}_s be the design points at node s , $s = 1, 2, 3$, and let Z_s be the computer code at node s . Let $\mathbf{V}^{(s,s)} = \text{Var}(Z_s(\mathcal{D}_s))$ be the covariance matrix of $Z_s(\mathcal{D}_s)$, and \mathbf{V}_s be the full covariance matrix of the data generated by the simulators from node 1 to node s . With the independence assumption between codes Z_1 and Z_2 , we have

$$\mathbf{V}_3 = \begin{bmatrix} \mathbf{V}^{(1,1)} & \mathbf{0} & \mathbf{U}^{(1,3)} \\ \mathbf{0} & \mathbf{V}^{(2,2)} & \mathbf{U}^{(2,3)} \\ \mathbf{U}^{(1,3)^T} & \mathbf{U}^{(2,3)^T} & \mathbf{V}^{(3,3)} \end{bmatrix} = \begin{bmatrix} \mathbf{V}_2 & \mathbf{U}_2 \\ \mathbf{U}_2^T & \mathbf{V}^{(3,3)} \end{bmatrix},$$

where \mathcal{D}_1 and \mathcal{D}_2 are ordered such that $\mathcal{D}_1 = [\mathcal{D}_1 \setminus \mathcal{D}_3, \mathcal{D}_3]$, $\mathcal{D}_2 = [\mathcal{D}_2 \setminus \mathcal{D}_3, \mathcal{D}_3]$, and

$\mathbf{U}_2 = [\mathbf{U}^{(1,3)}, \mathbf{U}^{(2,3)}]^T$. Here, $\mathbf{U}^{(1,3)}$ and $\mathbf{U}^{(2,3)}$ are covariances defined as:

$$\begin{cases} \mathbf{U}^{(1,3)} &= \text{Cov}(Z_1(\mathcal{D}_1), Z_3(\mathcal{D}_3)) \\ &= \text{Cov}(Z_1(\mathcal{D}_1), \boldsymbol{\rho}_1(\mathcal{D}_3) \odot Z_1(\mathcal{D}_3) + \boldsymbol{\rho}_2(\mathcal{D}_3) \odot Z_2(\mathcal{D}_3) + \delta_3(\mathcal{D}_3)) \\ &= (\mathbf{1}_{n_1} \boldsymbol{\rho}_1(\mathcal{D}_3)^T) \odot \text{Cov}(Z_1(\mathcal{D}_1), Z_1(\mathcal{D}_3)) \\ &= (\mathbf{1}_{n_1} \boldsymbol{\rho}_1(\mathcal{D}_3)^T) \odot \mathbf{V}^{(1,1)}(\mathcal{D}_1, \mathcal{D}_3) \\ \mathbf{U}^{(2,3)} &= (\mathbf{1}_{n_2} \boldsymbol{\rho}_2(\mathcal{D}_3)^T) \odot \mathbf{V}^{(2,2)}(\mathcal{D}_2, \mathcal{D}_3), \end{cases}$$

where $\mathbf{V}^{(1,1)}(\mathcal{D}_1, \mathcal{D}_3)$ and $\mathbf{V}^{(2,2)}(\mathcal{D}_2, \mathcal{D}_3)$ contain the last n_3 columns of $\mathbf{V}^{(1,1)}$ and $\mathbf{V}^{(2,2)}$, respectively.

Thus, $\mathbf{V}_2^{-1} \mathbf{U}_2$ can be simplified to

$$\begin{aligned} \mathbf{V}_2^{-1} \mathbf{U}_2 &= \begin{bmatrix} (\mathbf{V}^{(1,1)})^{-1} & \mathbf{0} \\ \mathbf{0} & (\mathbf{V}^{(2,2)})^{-1} \end{bmatrix} \begin{bmatrix} \mathbf{U}^{(1,3)} \\ \mathbf{U}^{(2,3)} \end{bmatrix} \\ &= \begin{bmatrix} (\mathbf{1}_{n_1} \boldsymbol{\rho}_1(\mathcal{D}_3)^T) \odot \begin{bmatrix} \mathbf{0}_{(n_1-n_3) \times n_3} \\ \mathbf{I}_{n_3} \end{bmatrix} \\ (\mathbf{1}_{n_2} \boldsymbol{\rho}_2(\mathcal{D}_3)^T) \odot \begin{bmatrix} \mathbf{0}_{(n_2-n_3) \times n_3} \\ \mathbf{I}_{n_3} \end{bmatrix} \end{bmatrix}. \end{aligned}$$

We then apply block matrix inversion to simplify \mathbf{V}_3^{-1} :

$$\mathbf{V}_3^{-1} = \begin{bmatrix} \mathbf{V}_2^{-1} + \mathbf{W}_{11} & \mathbf{W}_{12} \\ \mathbf{W}_{12}^T & \mathbf{W}_{22} \end{bmatrix} = \begin{bmatrix} \mathbf{V}_2^{-1} + \mathbf{V}_2^{-1} \mathbf{U}_2 \mathbf{Q}_3^{-1} \mathbf{U}_2^T \mathbf{V}_2^{-1} & -\mathbf{V}_2^{-1} \mathbf{U}_2 \mathbf{Q}_3^{-1} \\ -\mathbf{Q}_3^{-1} \mathbf{U}_2^T \mathbf{V}_2^{-1} & \mathbf{Q}_3^{-1} \end{bmatrix},$$

where

$$\mathbf{V}_2^{-1} = \begin{bmatrix} (\mathbf{V}^{(1,1)})^{-1} & \mathbf{0} \\ \mathbf{0} & (\mathbf{V}^{(2,2)})^{-1} \end{bmatrix},$$

$$\begin{aligned} \mathbf{W}_{22} &= \mathbf{Q}_3^{-1} = (\mathbf{V}^{(3,3)} - \mathbf{U}_2^T \mathbf{V}_2^{-1} \mathbf{U}_2)^{-1} = [\text{Cov}(Z_3(\mathcal{D}_3) | Z_1(\mathcal{D}_1), Z_2(\mathcal{D}_2))]^{-1} = [\text{Cov}(\delta_3(\mathcal{D}_3))]^{-1} \\ &= \frac{1}{\sigma_3^2} \cdot \mathbf{R}_3(\mathcal{D}_3)^{-1}, \end{aligned}$$

$$\mathbf{W}_{12} = -\mathbf{V}_2^{-1} \mathbf{U}_2 \mathbf{Q}_3^{-1} = - \begin{bmatrix} (\mathbf{1}_{n_1} \boldsymbol{\rho}_1(\mathcal{D}_3)^T) \odot \begin{bmatrix} \mathbf{0}_{(n_1-n_3) \times n_3} \\ \mathbf{I}_{n_3} \end{bmatrix} \\ (\mathbf{1}_{n_2} \boldsymbol{\rho}_2(\mathcal{D}_3)^T) \odot \begin{bmatrix} \mathbf{0}_{(n_2-n_3) \times n_3} \\ \mathbf{I}_{n_3} \end{bmatrix} \end{bmatrix} \cdot \frac{1}{\sigma_3^2} \cdot \mathbf{R}_3(\mathcal{D}_3)^{-1}$$

$$= - \begin{bmatrix} \mathbf{0}_{(n_1-n_3) \times n_3} \\ \frac{1}{\sigma_3^2}(\boldsymbol{\rho}_1(\mathcal{D}_3)\mathbf{1}_{n_3}^T) \odot \mathbf{R}_3(\mathcal{D}_3)^{-1} \\ \mathbf{0}_{(n_2-n_3) \times n_3} \\ \frac{1}{\sigma_3^2}(\boldsymbol{\rho}_2(\mathcal{D}_3)\mathbf{1}_{n_3}^T) \odot \mathbf{R}_3(\mathcal{D}_3)^{-1} \end{bmatrix},$$

$$\begin{aligned} \mathbf{W}_{11} &= \mathbf{V}_2^{-1} \mathbf{U}_2 \mathbf{Q}_3^{-1} \mathbf{U}_2^T \mathbf{V}_2^{-1} \\ &= \begin{bmatrix} \mathbf{0}_{(n_1-n_3) \times (n_1-n_3)} & \mathbf{0}_{(n_1-n_3) \times n_3} & \mathbf{0}_{(n_1-n_3) \times (n_2-n_3)} & \mathbf{0}_{(n_1-n_3) \times n_3} \\ \mathbf{0}_{n_3 \times (n_1-n_3)} & \frac{1}{\sigma_3^2}(\boldsymbol{\rho}_1(\mathcal{D}_3)\boldsymbol{\rho}_1(\mathcal{D}_3)^T) \odot \mathbf{R}_3(\mathcal{D}_3)^{-1} & \mathbf{0}_{n_3 \times (n_2-n_3)} & \frac{1}{\sigma_3^2}(\boldsymbol{\rho}_1(\mathcal{D}_3)\boldsymbol{\rho}_2(\mathcal{D}_3)^T) \odot \mathbf{R}_3(\mathcal{D}_3)^{-1} \\ \mathbf{0}_{(n_2-n_3) \times (n_1-n_3)} & \mathbf{0}_{(n_2-n_3) \times n_3} & \mathbf{0}_{(n_2-n_3) \times (n_2-n_3)} & \mathbf{0}_{(n_2-n_3) \times n_3} \\ \mathbf{0}_{n_3 \times (n_1-n_3)} & \frac{1}{\sigma_3^2}(\boldsymbol{\rho}_2(\mathcal{D}_3)\boldsymbol{\rho}_1(\mathcal{D}_3)^T) \odot \mathbf{R}_3(\mathcal{D}_3)^{-1} & \mathbf{0}_{n_3 \times (n_2-n_3)} & \frac{1}{\sigma_3^2}(\boldsymbol{\rho}_2(\mathcal{D}_3)\boldsymbol{\rho}_2(\mathcal{D}_3)^T) \odot \mathbf{R}_3(\mathcal{D}_3)^{-1} \end{bmatrix}. \end{aligned}$$

Next, we simplify the expression for $\mathbf{v}_3(\mathbf{x})^T \mathbf{V}_3^{-1}$, where $\mathbf{v}_3(\mathbf{x})$ is the covariance vector between $Z_3(\mathbf{x})$ and $\mathbf{z}^{(3)} = \{\mathbf{z}_1, \mathbf{z}_2, \mathbf{z}_3\}$ (observations at the three nodes). Then $\mathbf{v}_3(\mathbf{x}) = [\mathbf{v}_1^*(\mathbf{x}, \mathcal{D}_1)^T, \mathbf{v}_2^*(\mathbf{x}, \mathcal{D}_2)^T, \mathbf{v}_3^*(\mathbf{x}, \mathcal{D}_3)^T]^T$, where

$$\begin{cases} \mathbf{v}_1^*(\mathbf{x}, \mathcal{D}_1)^T &= \text{Cov}(Z_3(\mathbf{x}), Z_1(\mathcal{D}_1))^T = \rho_1(\mathbf{x}) \cdot \text{Cov}(Z_1(\mathbf{x}), Z_1(\mathcal{D}_1))^T = \sigma_1^2 \cdot \rho_1(\mathbf{x}) \cdot \mathbf{r}_1(\mathbf{x}, \mathcal{D}_1)^T \\ \mathbf{v}_2^*(\mathbf{x}, \mathcal{D}_2)^T &= \sigma_2^2 \cdot \rho_2(\mathbf{x}) \cdot \mathbf{r}_2(\mathbf{x}, \mathcal{D}_2)^T \\ \mathbf{v}_3^*(\mathbf{x}, \mathcal{D}_3)^T &= \boldsymbol{\rho}_1(\mathcal{D}_3) \odot \mathbf{v}_1^*(\mathbf{x}, \mathcal{D}_3)^T + \boldsymbol{\rho}_2(\mathcal{D}_3) \odot \mathbf{v}_2^*(\mathbf{x}, \mathcal{D}_3)^T + \sigma_3^2 \cdot \mathbf{r}_3(\mathbf{x}, \mathcal{D}_3)^T. \end{cases}$$

We can thus rewrite $\mathbf{v}_3(\mathbf{x})^T \mathbf{V}_3^{-1} = [\mathbf{A}, \mathbf{B}]$ where

$$\begin{cases} \mathbf{A} &= [\rho_1(\mathbf{x}) \cdot \mathbf{v}_1(\mathbf{x})^T (\mathbf{V}^{(1,1)})^{-1}, \rho_2(\mathbf{x}) \cdot \mathbf{v}_2(\mathbf{x})^T (\mathbf{V}^{(2,2)})^{-1}] \\ &\quad - [\mathbf{0}_{n_1-n_3}, (\boldsymbol{\rho}_1(\mathbf{x})^T \odot \mathbf{r}_3(\mathbf{x}, \mathcal{D}_3)) \mathbf{R}_3(\mathcal{D}_3)^{-1}, \mathbf{0}_{n_2-n_3}, (\boldsymbol{\rho}_2(\mathbf{x})^T \odot \mathbf{r}_3(\mathbf{x}, \mathcal{D}_3)) \mathbf{R}_3(\mathcal{D}_3)^{-1}] \\ \mathbf{B} &= \mathbf{r}_3(\mathbf{x}, \mathcal{D}_3) \mathbf{R}_3(\mathcal{D}_3)^{-1}. \end{cases}$$

Now, we show that the mean and covariance function of the GMGP model (6) match that for r-GMGP in (8). Let \mathbf{H}_3 be the matrix of basis functions and $\boldsymbol{\beta} = \{\boldsymbol{\beta}_1, \boldsymbol{\beta}_2, \boldsymbol{\beta}_3\}$ be the vector of coefficients such that $\mathbf{H}_3 \boldsymbol{\beta}$ gives the prior mean of $\mathbf{z}^{(3)}$. Then \mathbf{H}_3 is given by:

$$\mathbf{H}_3 = \begin{bmatrix} \mathbf{h}_1(\mathcal{D}_1)^T & \mathbf{0} & \mathbf{0} \\ \mathbf{0} & \mathbf{h}_2(\mathcal{D}_2)^T & \mathbf{0} \\ \boldsymbol{\rho}_1(\mathcal{D}_3) \odot \mathbf{h}_1(\mathcal{D}_3)^T & \boldsymbol{\rho}_2(\mathcal{D}_3) \odot \mathbf{h}_2(\mathcal{D}_3)^T & \mathbf{h}_3(\mathcal{D}_3)^T \end{bmatrix}.$$

Under a similar definition, we have $\mathbf{H}_1 = \mathbf{h}_1(\mathcal{D}_1)^T$ and $\mathbf{H}_2 = \mathbf{h}_2(\mathcal{D}_2)^T$ such that the prior means of \mathbf{z}_1 and \mathbf{z}_2 are given by $\mathbf{H}_1 \boldsymbol{\beta}_1$ and $\mathbf{H}_2 \boldsymbol{\beta}_2$, respectively. Using the above formula for $\mathbf{v}_3(\mathbf{x})^T \mathbf{V}_3^{-1}$, we thus have

$$\begin{aligned} \mathbf{v}_3(\mathbf{x})^T \mathbf{V}_3^{-1} \mathbf{z}^{(3)} &= \rho_1(\mathbf{x}) \cdot \mathbf{v}_1(\mathbf{x})^T (\mathbf{V}^{(1,1)})^{-1} \mathbf{z}_1 + \rho_2(\mathbf{x}) \cdot \mathbf{v}_2(\mathbf{x})^T (\mathbf{V}^{(2,2)})^{-1} \mathbf{z}_2 \\ &\quad - (\boldsymbol{\rho}_1(\mathcal{D}_3) \odot \mathbf{r}_3(\mathbf{x}, \mathcal{D}_3)) \mathbf{R}_3(\mathcal{D}_3)^{-1} \mathbf{z}_1(\mathcal{D}_3) - (\boldsymbol{\rho}_2(\mathcal{D}_3) \odot \mathbf{r}_3(\mathbf{x}, \mathcal{D}_3)) \mathbf{R}_3(\mathcal{D}_3)^{-1} \mathbf{z}_2(\mathcal{D}_3) \end{aligned}$$

$$\begin{aligned}
& + \mathbf{r}_3(\mathbf{x}, \mathcal{D}_3) \mathbf{R}_3(\mathcal{D}_3)^{-1} \mathbf{z}_3, \\
\mathbf{v}_3(\mathbf{x})^T \mathbf{V}_3^{-1} \mathbf{H}_3 \boldsymbol{\beta} &= \rho_1(\mathbf{x}) \cdot \mathbf{v}_1(\mathbf{x})^T (\mathbf{V}^{(1,1)})^{-1} \mathbf{H}_1 \boldsymbol{\beta}_1 + \rho_2(\mathbf{x}) \cdot \mathbf{v}_2(\mathbf{x})^T (\mathbf{V}^{(2,2)})^{-1} \mathbf{H}_2 \boldsymbol{\beta}_2 \\
& + \mathbf{r}_3(\mathbf{x}, \mathcal{D}_3) \mathbf{R}_3(\mathcal{D}_3)^{-1} \mathbf{h}_3(\mathcal{D}_3)^T \boldsymbol{\beta}_3, \\
\mathbf{v}_3(\mathbf{x})^T \mathbf{V}_3^{-1} \mathbf{v}_3(\mathbf{x}) &= \rho_1(\mathbf{x})^2 \mathbf{v}_1(\mathbf{x})^T (\mathbf{V}^{(1,1)})^{-1} \mathbf{v}_1(\mathbf{x}) + \rho_2(\mathbf{x})^2 \mathbf{v}_2(\mathbf{x})^T (\mathbf{V}^{(2,2)})^{-1} \mathbf{v}_2(\mathbf{x}) \\
& + \sigma_3^2 \mathbf{r}_3(\mathbf{x}, \mathcal{D}_3) \mathbf{R}_3(\mathcal{D}_3)^{-1} \mathbf{r}_3(\mathbf{x}, \mathcal{D}_3)^T.
\end{aligned}$$

With this, we can now show the equivalence of predictive means and variances for the GMGP and r-GMGP models (from equations (6) and (8) in the main paper):

$$\begin{aligned}
\mu_{Z_3}(\mathbf{x}) &= \left[\sum_{t' \in Pa(3)} \rho_{t'}(\mathbf{x}) \mathbf{h}_{t'}(\mathbf{x})^T \boldsymbol{\beta}_{t'} + \mathbf{h}_3(\mathbf{x})^T \boldsymbol{\beta}_3 \right] + \mathbf{v}_3(\mathbf{x})^T \mathbf{V}_3^{-1} (\mathbf{z}^{(3)} - \mathbf{H}_3 \boldsymbol{\beta}) \\
&= \rho_1(\mathbf{x}) \mathbf{h}_1(\mathbf{x})^T \boldsymbol{\beta}_1 + \rho_2(\mathbf{x}) \mathbf{h}_2(\mathbf{x})^T \boldsymbol{\beta}_2 + \mathbf{h}_3(\mathbf{x})^T \boldsymbol{\beta}_3 \\
&\quad + \rho_1(\mathbf{x}) \mathbf{v}_1(\mathbf{x})^T (\mathbf{V}^{(1,1)})^{-1} (\mathbf{z}_1 - \mathbf{H}_1 \boldsymbol{\beta}_1) + \rho_2(\mathbf{x}) \mathbf{v}_2(\mathbf{x})^T (\mathbf{V}^{(2,2)})^{-1} (\mathbf{z}_2 - \mathbf{H}_2 \boldsymbol{\beta}_2) \\
&\quad + \mathbf{r}_3(\mathbf{x}, \mathcal{D}_3) \mathbf{R}_3(\mathcal{D}_3)^{-1} [\mathbf{z}_3 - \boldsymbol{\rho}_1(\mathcal{D}_3) \odot \mathbf{z}_1(\mathcal{D}_3) - \boldsymbol{\rho}_2(\mathcal{D}_3) \odot \mathbf{z}_2(\mathcal{D}_3) - \mathbf{h}_3(\mathcal{D}_3)^T \boldsymbol{\beta}_3] \\
&= [\rho_1(\mathbf{x}) \mu_{Z_1}(\mathbf{x}) + \rho_2(\mathbf{x}) \mu_{Z_2}(\mathbf{x}) + \mathbf{h}_3(\mathbf{x})^T \boldsymbol{\beta}_3] \\
&\quad + \mathbf{r}_3(\mathbf{x}, \mathcal{D}_3) \mathbf{R}_3(\mathcal{D}_3)^{-1} [\mathbf{z}_3 - \boldsymbol{\rho}_1(\mathcal{D}_3) \odot \mathbf{z}_1(\mathcal{D}_3) - \boldsymbol{\rho}_2(\mathcal{D}_3) \odot \mathbf{z}_2(\mathcal{D}_3) - \mathbf{h}_3(\mathcal{D}_3)^T \boldsymbol{\beta}_3],
\end{aligned}$$

$$\begin{aligned}
\sigma_{Z_3}^2(\mathbf{x}) &= v_{Z_3}^2(\mathbf{x}) - \mathbf{v}_3(\mathbf{x})^T \mathbf{V}_3^{-1} \mathbf{v}_3(\mathbf{x}) \\
&= \rho_1^2(\mathbf{x}) \sigma_1^2 + \rho_2^2(\mathbf{x}) \sigma_2^2 + \sigma_3^2 - \rho_1^2(\mathbf{x}) \mathbf{v}_1(\mathbf{x})^T (\mathbf{V}^{(1,1)})^{-1} \mathbf{v}_1(\mathbf{x}) \\
&\quad - \rho_2^2(\mathbf{x}) \mathbf{v}_2(\mathbf{x})^T (\mathbf{V}^{(2,2)})^{-1} \mathbf{v}_2(\mathbf{x}) - \sigma_3^2 \mathbf{r}_3(\mathbf{x}, \mathcal{D}_3) \mathbf{R}_3(\mathcal{D}_3)^{-1} \mathbf{r}_3(\mathbf{x}, \mathcal{D}_3)^T \\
&= \rho_1^2(\mathbf{x}) \sigma_{Z_1}^2(\mathbf{x}) + \rho_2^2(\mathbf{x}) \sigma_{Z_2}^2(\mathbf{x}) + \sigma_3^2 [1 - \mathbf{r}_3(\mathbf{x}, \mathcal{D}_3)^T \mathbf{R}_3(\mathcal{D}_3)^{-1} \mathbf{r}_3(\mathbf{x}, \mathcal{D}_3)].
\end{aligned}$$

As shown above, the same recursive relation holds between $\mu_{Z_3}(\mathbf{x})$ and $m_{Z_3}(\mathbf{x})$, and between $\sigma_{Z_3}^2(\mathbf{x})$ and $s_{Z_3}^2(\mathbf{x})$ when the training data are nested and noise-free. Thus we have $\mu_{Z_3}(\mathbf{x}) = m_{Z_3}(\mathbf{x})$ and $\sigma_{Z_3}^2(\mathbf{x}) = s_{Z_3}^2(\mathbf{x})$. With the assumption that all source nodes are independent, one can extend the proof approach in a straight-forward manner for in-trees of depth 2 with more than two source nodes.

B.2 Connecting sub-graphs

Now, let us consider a more complicated DAG which connects several lower-level in-trees. Again, we show the mean and variance equivalence using the simplest case and extend it to in-trees with more branches. Let node A and B be the root nodes of two lower-level in-trees, which we will call them Tree A and Tree B , respectively. Node A, B, C forms a larger in-tree and node C is the child node. Figure 12a shows connections between Tree A

and Node C , Tree B and Node C .

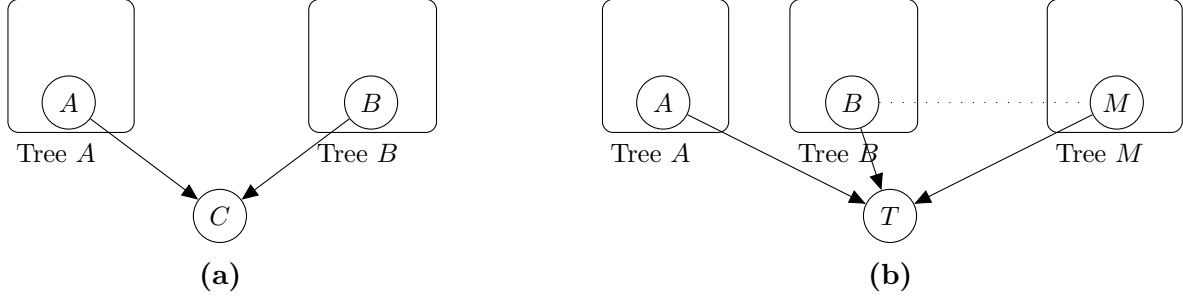


Figure 12: In-trees constructed by: (left) connecting 2 lower-level in-trees; (right) connecting $M > 2$ lower-level in-trees.

Again, we reorder the nested design sets such that $\mathcal{D}_A = [\mathcal{D}_A \setminus \mathcal{D}_C, \mathcal{D}_C]$, $\mathcal{D}_B = [\mathcal{D}_B \setminus \mathcal{D}_C, \mathcal{D}_C]$. With the independence assumption between Tree A and Tree B, we have the following full covariance matrix:

$$\mathbf{V}_C = \begin{bmatrix} \mathbf{V}_A & \mathbf{0} & \mathbf{U}^{(A,C)} \\ \mathbf{0} & \mathbf{V}_B & \mathbf{U}^{(B,C)} \\ \mathbf{U}^{(A,C)^T} & \mathbf{U}^{(B,C)^T} & \mathbf{V}^{(C,C)} \end{bmatrix},$$

where \mathbf{V}_A and \mathbf{V}_B are covariance matrices of Tree A and B, respectively. Let $\{Z_{A_i}\}_{A_i \in \text{Anc}(A)}$ be the non-root nodes in Tree A (with A being the root node), we have

$$\mathbf{U}^{(A,C)} = \begin{bmatrix} \text{Cov}(Z_{A_1}(\mathcal{D}_{A_1}), Z_C(\mathcal{D}_C)) \\ \text{Cov}(Z_{A_2}(\mathcal{D}_{A_2}), Z_C(\mathcal{D}_C)) \\ \dots \\ \text{Cov}(Z_A(\mathcal{D}_A), Z_C(\mathcal{D}_C)) \end{bmatrix},$$

where

$$\begin{aligned} \text{Cov}(Z_{A_i}(\mathcal{D}_{A_i}), Z_C(\mathcal{D}_C)) &= \text{Cov}(Z_{A_i}(\mathcal{D}_{A_i}), \boldsymbol{\rho}_A(\mathcal{D}_C) \odot Z_A(\mathcal{D}_C) + \boldsymbol{\rho}_B(\mathcal{D}_C) \odot Z_B(\mathcal{D}_C) + \delta_C(\mathcal{D}_C)) \\ &= \text{Cov}(Z_{A_i}(\mathcal{D}_{A_i}), \boldsymbol{\rho}_A(\mathcal{D}_C) \odot Z_A(\mathcal{D}_C)) \\ &= (\mathbf{1}_{n_{A_i}} \boldsymbol{\rho}_A(\mathcal{D}_C)^T) \odot \text{Cov}(Z_{A_i}(\mathcal{D}_{A_i}), Z_A(\mathcal{D}_C)) \\ &= (\mathbf{1}_{n_{A_i}} \boldsymbol{\rho}_A(\mathcal{D}_C)^T) \odot \mathbf{V}^{(A_i,A)}(\mathcal{D}_{A_i}, \mathcal{D}_C). \end{aligned}$$

Thus

$$\begin{aligned} \mathbf{U}^{(A,C)} &= (\mathbf{1}_{(\sum_{A_i \in \text{Anc}(A)} n_{A_i} + n_A)} \boldsymbol{\rho}_A(\mathcal{D}_C)^T) \odot \begin{bmatrix} \mathbf{V}^{(A_1,A)}(\mathcal{D}_{A_1}, \mathcal{D}_C) \\ \mathbf{V}^{(A_2,A)}(\mathcal{D}_{A_2}, \mathcal{D}_C) \\ \dots \\ \mathbf{V}^{(A,A)}(\mathcal{D}_A, \mathcal{D}_C) \end{bmatrix} \\ &= (\mathbf{1}_{(\sum_{A_i \in \text{Anc}(A)} n_{A_i} + n_A)} \boldsymbol{\rho}_A(\mathcal{D}_C)^T) \odot \mathbf{V}_A^{n_C}, \end{aligned}$$

where $\mathbf{V}_A^{n_C}$ refers to the last n_C columns of \mathbf{V}_A . With the same calculation for $\mathbf{U}^{(B,C)}$, we have

$$\begin{bmatrix} \mathbf{V}_A & \mathbf{0} \\ \mathbf{0} & \mathbf{V}_B \end{bmatrix}^{-1} \begin{bmatrix} \mathbf{U}^{(A,C)} \\ \mathbf{U}^{(B,C)} \end{bmatrix} = \begin{bmatrix} (\mathbf{1}_{(\sum_{A_i \in \text{Anc}(A)} n_{A_i} + n_A)} \boldsymbol{\rho}_A(\mathcal{D}_C)^T) \odot \begin{bmatrix} \mathbf{0}_{((\sum_{A_i \in \text{Anc}(A)} n_{A_i} + n_A) - n_C) \times n_C} \\ \mathbf{I}_{n_C} \end{bmatrix} \\ (\mathbf{1}_{(\sum_{B_j \in \text{Anc}(B)} n_{B_j} + n_B)} \boldsymbol{\rho}_B(\mathcal{D}_C)^T) \odot \begin{bmatrix} \mathbf{0}_{((\sum_{B_j \in \text{Anc}(B)} n_{B_j} + n_B) - n_C) \times n_C} \\ \mathbf{I}_{n_C} \end{bmatrix} \end{bmatrix}.$$

We observe that the above expression is comparable to $\mathbf{V}_2^{-1} \mathbf{U}_2$ defined in previous section. Similarly, using the same definition of matrix \mathbf{Q}_C , we see that it is comparable to \mathbf{Q}_3 : $\mathbf{Q}_C = \text{Cov}(Z_C(\mathcal{D}_C) | \text{Tree } A, \text{Tree } B) = \sigma_C^2 \mathbf{R}_C(\mathcal{D}_C)$.

Following the same derivation as in previous section, we are able to show $\mu_{Z_C}(\mathbf{x}) = m_{Z_C}(\mathbf{x})$ and $\sigma_{Z_C}^2(\mathbf{x}) = s_{Z_C}^2(\mathbf{x})$. The above proof can also be naturally generalized to a more complicated in-tree where we have multiple lower-level in-trees connecting to a new root node. Finally, note that all directed in-trees can be recursively constructed by connecting lower-level in-trees to a new root node. This completes the proof of the equivalence for the posterior mean and variance of GMGP and r-GMGP when the multi-fidelity DAG \mathcal{G} is a directed in-tree.